

Template shape estimation: correcting an asymptotic bias

Nina Miolane^{1,2*}, Susan Holmes², Xavier Pennec¹,

¹ INRIA, Asclepios project-team, 2004 Route des Lucioles, BP93, F-06902 Sophia Antipolis Cedex, France,
nina.miolane@inria.fr, +33 4 92 38 71 82,

² Stanford University, Department of Statistics, Sequoia Hall, Serra Mall, Stanford CA

Abstract. We use tools from geometric statistics to analyze the usual estimation procedure of a template shape. This applies to shapes from landmarks, curves, surfaces, images etc. We demonstrate the asymptotic bias of the template shape estimation using the stratified geometry of the shape space. We give a Taylor expansion of the bias with respect to a parameter σ describing the measurement error on the data. We propose two bootstrap procedures that quantify the bias and correct it, if needed. They are applicable for any type of shape data. We give a rule of thumb to provide intuition on whether the bias has to be corrected. This exhibits the parameters that control the bias' magnitude. We illustrate our results on simulated and real shape data.

Keywords: shape, template, quotient space, manifold

Introduction

The shape of a set of points, the shape of a signal, the shape of a surface, or the shapes in an image can be defined as follows: the remainder after we have filtered out the position and the orientation of the object [17]. Statistics on shapes appear in many fields. Paleontologists combine shape analysis of monkey skulls with ecological and biogeographic data to understand how the *skull shapes* have changed in space and time during evolution [12]. Molecular Biologists study how *shapes of proteins* are related to their function. Statistics on misfolding of proteins is used to understand diseases, like Parkinson's disease [21]. Orthopaedic surgeons analyze *bones' shapes* for surgical pre-planning [9]. In Signal processing, the *shape of neural spike trains* correlates with arm movement [18]. In Computer Vision, classifying *shapes of handwritten digits* enables automatic reading of texts [4]. In Medical Imaging and more precisely in Neuroimaging, studying *brain shapes* as they appear in the MRIs facilitates discoveries on diseases, like Alzheimer [22].

What do these applications have in common? Position and orientation of the skulls, proteins, bones, neural spike trains, handwritten digits or brains do not matter for the study's goal: only *shapes* matter. Mathematically, the study analyses the statistical distributions of *the equivalence classes of the data* under translations and rotations. They project the data in a quotient space, called the *shape space*.

The simplest - and most widely used - method for summarizing shapes is the computation of the mean shape. Almost all neuroimaging studies start with the computation of the mean brain shape [13] for example. One refers to the mean shape with different terms depending on the field: mean configuration, mean pattern, template, atlas, etc. The mean shape is an average of *equivalence classes of the data*: one computes the mean after projection of the data in the shape space. One may wonder if the projection biases the statistical procedure. This is a legitimate question as any bias introduced with this step would make the conclusions of the study less accurate. If the mean brain shape is biased, then neuroimaging's inferences on brain diseases will be too. This paper shows that a bias is indeed introduced for the mean shape estimation under certain conditions.

Related work

We review works on the shape space’s geometry as a quotient space, and existing results on the mean shape’s bias.

Shapes of landmarks: Kendall analyses The theory for shapes *of landmarks* is introduced by Kendall in the 1980’s [16]. He considers shapes of k labeled landmarks in \mathbb{R}^m . The size-and-shape space, written $S\Sigma_m^k$, takes also into account the overall size of the landmarks’ set. The shape space, written Σ_m^k , quotients by the size as well. Both $S\Sigma_m^k$ and Σ_m^k have a Riemannian geometry, whose metrics are given in [19]. These studies model the probability distribution of the data directly in the shape space Σ_m^k . They do not consider that the data are observed in the space of landmarks $(\mathbb{R}^m)^k$ and projected in the shape space Σ_m^k . The question of the bias is not raised.

Shapes of landmarks: Procrustean analyses Procrustean analysis is related to Kendall shape spaces but it also considers shapes of landmarks [10]. Kendall analyses project the data in the shape space by explicitly computing their coordinates in Σ_m^k . In contrast, Procrustean analyses keep the coordinates in $(\mathbb{R}^m)^k$: they project the data in the shape space by ”aligning” or ”registering” them. Orthogonal Procrustes analysis ”aligns” the sets of landmarks by rotating each set to minimize the Euclidean distance to the other sets. Procrustean analysis considers the fact that the data are observed in the space $(\mathbb{R}^m)^k$ but does not consider the geometry of the shape space. The bias on the mean shape is shown in [20] with a *reducto ad absurdum* proof. But there is no geometric intuition given about how to control or correct the phenomenon.

Shapes of curves The curve data are projected in their shape space by an alignment step [15], in the spirit of a Procrustean analysis. The bias of the mean shape is discussed in the literature. Unbiasedness was shown for shapes of signals in [18] but under the simplifying assumption of no measurement error on the data. Some authors provide examples of bias when there is measurement error [2]. Their experiments show that the mean signal shape may converge to pure noise when the measurement error on simulated signals increases. The bias is proven in [6] for curves estimated from a finite number of points in the presence of error. But again, no geometric intuition nor correction strategy is given.

Contributions and outline

We are missing a global geometric understanding of the bias. Which variables control its magnitude? Is it restricted to the mean shape or does it appear for other statistical analyses? How important is it in practice: do we even need to correct it? If so, how can we correct it? Our paper is addressing these questions. We use a geometric framework that unifies the cases of landmarks, curves, images etc.

Contributions We make three contributions. First, we show that statistics on shapes are biased when the data are measured with error. We explicitly compute the bias in the case of the mean shape. Second, we offer an interpretation of the bias through the geometry of the shape space. In applications, this aids in deciding when the bias can be neglected in contrast with situations when it must be corrected. Third, we leverage our understanding to suggest several correction approaches.

Outline The paper has four Sections. Section 1 introduces the geometric framework of shape spaces. Section 2 presents our first two contributions: the proof and geometric interpretation of the bias. Section 3 describes our third contribution: the procedures to correct the bias. Section 4 validates and illustrates our results on synthetic and real data.

1 Geometrization of template shape estimation

1.1 Two running examples

We introduce two simple examples of shape spaces. We will refer to them constantly to provide intuition.

First, we consider two landmarks in the plane \mathbb{R}^2 (Figure 1 (a)). The landmarks are parameterized each with 2 coordinates. For simplicity we consider that one landmark is fixed at the origin on \mathbb{R}^2 . Thus the system is now parameterized by the 2 coordinates of the second landmark only, e.g. in polar coordinates (r, θ) . We are interested in the shape of the 2 landmarks, i.e. in their distance which is simply r .

Second, we consider two landmarks on the sphere S^2 (Figure 1 (b)). One of the landmark is fixed at the origin of S^2 . The system is now parameterized by the 2 coordinates of the second landmark only, i.e. (θ, ϕ) . The shape of the two landmarks is the angle between them and is simply θ .

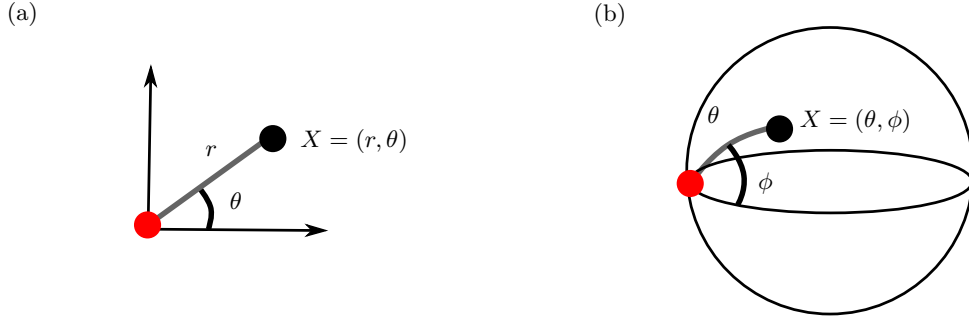


Fig. 1. Two landmarks, one in red and one in black, on the plane \mathbb{R}^2 (a) and on the sphere S^2 (b). The landmark in red is fixed at the origin of the coordinates. The system is entirely represented by the coordinates X of the landmark in black.

1.2 Differential Geometry of shapes

The shape space is a quotient space The data are objects $\{X_i\}_{i=1}^n$ that are either sets of landmarks, curves, images, etc. We consider that each object X_i is a point in a Riemannian manifold M . We restrict in this paper to finite dimensional manifolds in order to avoid complications. We have $M = \mathbb{R}^2$ in the plane example: a flat manifold of dimension 2. We have $M = S^2$ in the sphere example: a manifold of constant positive curvature and of dimension 2.

By definition, the objects' shapes are their equivalence classes $\{[X_i]\}_{i=1}^n$ under the action of some finite dimensional Lie group G : G is a group of continuous transformations that models what does not change the shape. The action of G on M will be written with \cdot . In our examples, the rotations are the transformations that leave the shape of the systems invariant. Let us take g a rotation. The action of g on the landmark X is illustrated by a blue arrow in Figures 2 (a) for the plane and (d) for the sphere. We observe that the action does not change the shape of the systems: the distance between the two landmarks is preserved in (a), the angle between the two landmarks is preserved in (d). The equivalence class of X_i is also called its orbit and written O_{X_i} . The equivalence class/orbit of X is illustrated with the blue dotted circle in Figure 2 (a) for the plane example and in Figure 2 (b) for the sphere example. The orbit of X in M is the submanifold of all objects in M that have the same shape as X . The curvature of the orbit as a submanifold of M is the key point of the results in Section 2.

The *shape space* is by definition the space of orbits. This is a quotient space denoted $Q = M/G$. One orbit in M , i.e. one circle in Figure 2 (b) or (e), corresponds to a point in Q . The shape space is $Q = \mathbb{R}_+$ in the plane example. This is the space of all possible distances between the two landmarks, see Figure 2 (c). The shape space is $Q = [0, \pi]$ in the sphere example. This is the space of all possible angles between the two landmarks, see Figure 2 (f).

The shape space is a metric space We consider that the action of G on M is *isometric with respect to the Riemannian metric of M* . This implies that the distance d_M between two objects in M does not change if we transform both objects in the same manner. In the plane example, rotating the landmark X_1 and another landmark X_2 with the same angle does not change the distance between them.

The distance in M induces a quasi-distance d_Q in Q : $d_Q(O_{X_1}, O_{X_2}) = \inf_{g \in G} d_M(g \cdot X_1, X_2)$. The distance between the shapes of X_1 and X_2 is computed by first registering/aligning X_1 onto X_2 by the mean of g , and then using the distance in the ambient space M . In the plane example, the distance between two shapes is the difference in distances between the landmarks. One can compute it by first aligning the landmarks, say on the first axis of \mathbb{R}^2 . Then, one uses the distance in \mathbb{R}^2 .

The shape space is stratified Both object space M and shape space Q are stratified because of the notion of isotropy group. The *isotropy group of X_i* is the subgroup of transformations of G that leave X_i invariant. For the plane example, every $X_i \neq (0, 0)$ has isotropy group the identity and $(0, 0)$ has isotropy group the whole group of 2D rotations. Objects on the same orbit, i.e. objects that have the same shape, have conjugate isotropy groups. The *orbit type* of an orbit is the corresponding conjugate class.

Principal shapes are shapes with smallest isotropy group conjugation class. In the plane example, $\mathbb{R}^2 \setminus (0, 0)$ is the set of objects with principal shapes. It corresponds to \mathbb{R}_+^* in the shape space and is colored in blue on Figure 2 (c). *Singular shapes* are shapes with larger isotropy group conjugation class. In the plane example, $(0, 0)$ is the only object with singular shape. It corresponds to 0 in \mathbb{R}_+ and is colored in red in Figure 2 (c).

The (connected components of) the *orbit types* form a stratification of M , called the *orbit-type stratification of M* . The principal type is predominant in the following sense: the set of principal strata, which we denote M^* , is open and dense in M . This means that there are objects with non-degenerated shapes almost everywhere.

The stratification of M into orbit types strata gives a stratification of the shape space M/G . Also, non-degenerated shapes are dense in the shape space.

We have focused on an intuitive introduction of the concepts. We refer to [29,1,14] for mathematical details. From now on, the mathematical setting is the following: we assume a proper, effective and isometric action of a finite dimensional Lie group G on a finite dimensional Riemannian manifold M .

1.3 Geometrization of generative models of shape data

We recall that the data are the $\{X_i\}_{i=1}^n$ that are sets of landmarks, curves, images, etc. We interpret the data X_i 's as random realizations of the generative model:

$$X_i = \text{Exp}(g_i \cdot Y_i, \epsilon_i) \quad i = 1 \dots n, \quad (1)$$

where the observed object $X_i \in M$ is a shape $Y_i \in M/G \subset M$ with a given position or parameterization $g_i \in G$ and observed with noise $\epsilon_i \in T_{g_i \cdot Y_i} M$. Here $\text{Exp}(p, u)$ denotes the

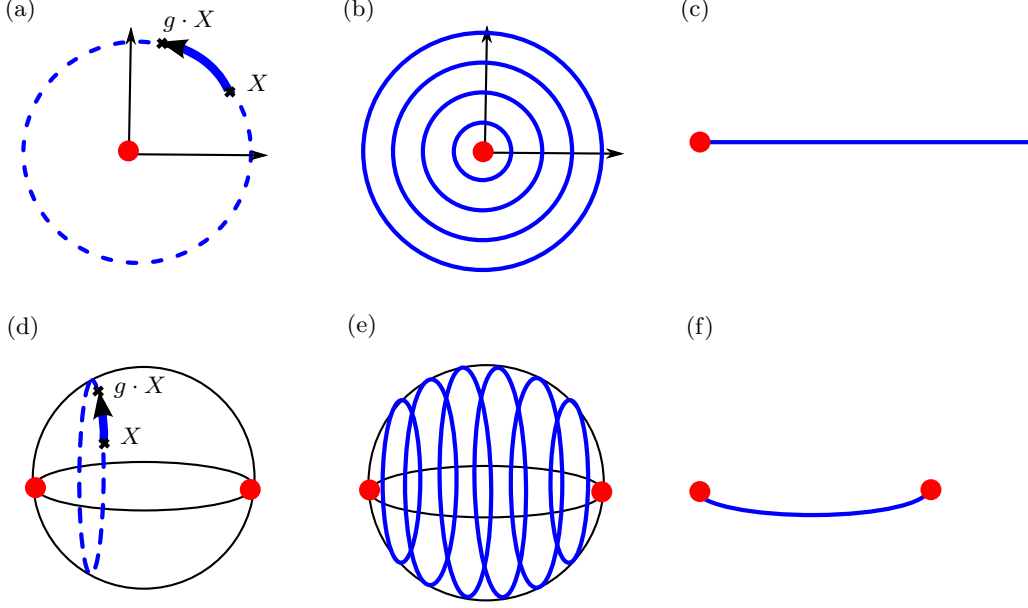


Fig. 2. First line: Action of rotations on \mathbb{R}^2 , with (a): action of rotation $g \in SO(2)$ on point $X \in \mathbb{R}^2$ and orbit of X in blue dotted line; (b) Stratification of \mathbb{R}^2 into principal orbit type (blue) and singular orbit type (red); (c) shape space $\mathbb{R}_+ = \mathbb{R}^2/SO(2)$ with a singularity (red dot). Second line: Action of $SO(2)$ on S^2 with (d): action of rotation $g \in SO(2)$ on point $X \in S^2$ and orbit of X in blue dotted line; (e) Stratification of S^2 into principal orbit type (blue) and singular orbit type (red) (f) shape space $[0, \pi] = S^2/SO(2)$ with two singularities (red dots).

Riemannian exponential of u at point p . The Y_i, g_i, ϵ_i are themselves i.i.d. realizations of random variables. Drawing them lead to the following three step interpretation of the generative model 1.

Step 1: Generate the shape $Y_i \in M/G$ We assume that there is an probability density of shapes in $Q = M/G$, with respect to the measure on Q induced by the Riemannian measure of M . The Y_i 's are i.i.d. samples drawn from this distribution. For example, it can be a Gaussian as illustrated in Figure 3 on the shape spaces for the plane and sphere examples. This is the variability that is meaningful for the statistical study, whether we are analyzing shapes of skulls, proteins, bones, neural spike trains, handwritten digits or brains. We assume in this paper that the distribution is simply a Dirac at Y which we call the *template shape*. This is the most common assumption in these generative models [2,?, ?, ?].



Fig. 3. Step 1 of generative model 1 for the plane example (a) and the sphere example (b). The black curve illustrates the probability distribution function on shape space. This is a distribution on $r \in \mathbb{R}_+$ for the plane example (a) and on $\theta \in [0, \pi]$ for the sphere example. The black square represents its expectation.

Step 2: Generate its position/parameterization $g_i \in G$ We cannot observe shapes in $Q = M/G$. We rather observe objects in M , that are shapes posed or parameterized in a certain way. We assume that there is a probability distribution on the positions or parameterizations of G , or equivalently a probability distribution on principal orbits with respect to their intrinsic measure. We assume that the distribution does not depend on the shape Y_i that has been drawn. The g_i 's are i.i.d. from this distribution. For example, it can be a Gaussian as illustrated in Figure 4 on the shape spaces for the plane and sphere examples.

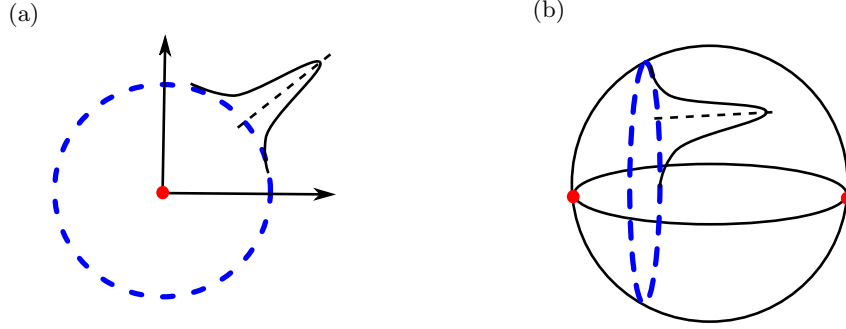


Fig. 4. Step 2 of generative model 1 for the plane example (a) and the sphere example (b). The blue dotted curve illustrates the orbit of the shape drawn in Step 1. The black curve illustrates the probability distribution function on this orbit. This is a distribution in angle $\theta \in [0, 2\pi]$ for the plane example (polar coordinates) and in angle $\phi \in [0, 2\pi]$ for the sphere example (spherical coordinates).

Step 3: Generate the noise $\epsilon_i \in T_{g_i \cdot Y_i} M$ The observed X_i 's are results of noisy measurements. We assume that there is a probability distribution function on $T_{g_i \cdot Y_i} M$ representing the noise. We further assume that this is a Gaussian centered at $g_i \cdot Y_i$, the origin of the tangent space $T_{g_i \cdot Y_i} M$, and with standard deviation σ , see Figures 5. The parameter σ will be extremely important in the developments of Section, as we will compute Taylor expansions around $\sigma = 0$.

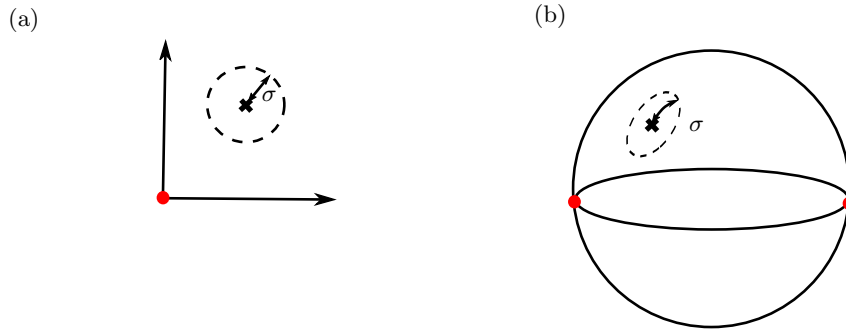


Fig. 5. Step 2 of generative model 1 for the plane example (a) and the sphere example (b). The dotted curve represents the isolevel at σ of the Gaussian distribution function on the ambient space.

Other generative models may be considered in the literature. We find in [3] the model: $X_i = g_i \cdot \text{Exp}(Y_i, \epsilon_i)$ and in [18] the model: $X_i = g_i \cdot Y_i$.

1.4 Learning the variability in shapes: estimating the template shape

Our goal is to unveil the variability of shapes in $Q = M/G$ while we in fact observe the noisy objects X_i 's in M . First, we focus on the case where the variability in the shape space is assumed to be a Dirac at Y (Step 1 of generative model). Our goal is thus to estimate the template shape Y .

One may consider the Maximum Likelihood estimate of Y :

$$\begin{aligned}\hat{Y}_{ML} &= \operatorname{argmax}_{Y \in Q} L(Y) = \operatorname{argmax}_{Y \in Q} \sum_{i=1}^n \log(P(X_i|Y)) \\ &= \operatorname{argmax}_{Y \in Q} \sum_{i=1}^n \log \left(\int_{g \in G} P(X_i|Y, g) \cdot P(g) dg \right).\end{aligned}$$

We have hidden variables, the g 's. The Expectation-Maximization (EM) algorithm would be the natural implementation for computing the ML estimator. But the EM algorithm is computationally expensive, above all for tridimensional images. Thus, one usually relies on another procedure that is an approximation of the EM. [2,3,18,7].

Estimating the template shape with the Fréchet mean in the shape space One initializes the estimate with $\hat{Y} = X_1$. Then, one iterates the following two steps until convergence:

$$(1) \quad \hat{g}_i = \operatorname{argmin}_{g \in G} d_M(\hat{Y}, g \cdot X_i), \quad \forall i \in \{1, \dots, n\},$$

$$(2) \quad \hat{Y} = \operatorname{argmin}_{Y \in M} \sum_{i=1}^n d_M(Y, \hat{g}_i \cdot X_i)^2.$$

(1) is an estimation of the hidden observations g_i and an approximation of the E-step of the EM algorithm. (2) is the M-step of the EM algorithm: the maximization of the surrogate in the M-step amounts to the maximization of the variance of the projected data. This is exactly the minimization of the squared distances to the data of (2).

The procedure converges because it decreases at each step a cost bounded below by zero. The estimator computed with this procedure is:

$$\hat{Y} = \operatorname{argmin}_{Y \in M} \sum_{i=1}^n \min_{g \in G} d_M^2(Y, g \cdot X_i). \quad (2)$$

The term $\min_{g \in G} d_M^2(Y, g \cdot X_i)$ in Equation 2 is the distance in the shape space between the shapes of Y and X_i . Thus, we recognize in Equation 2 the Fréchet mean on the shape space. The Fréchet mean is a definition of mean on manifolds [27]: it is the point that minimizes the squared distances to the data in the shape space. All in all, one projects the probability distribution function of the X_i 's from M to M/G and computes its "expectation", in a sense made precise later.

We illustrate the procedure with the examples of the plane and the sphere. We take X_1, X_2, X_3 three objects in \mathbb{R}^2 in Figure 6 (a) and on S^2 in Figure 6 (b). Step (1) is the registration/alignment step. One filters out the position/parameterization component, i.e. the coordinate on the orbit. One projects the objects X_1, X_2, X_3 in the shape space Q using the blue arrows. Step (2) is the computation of the Fréchet mean of the registered data.

We implemented the generative model and the estimation procedure on the plane and the sphere in shiny applications available online: <https://nmiolane.shinyapps.io/shinyPlane>

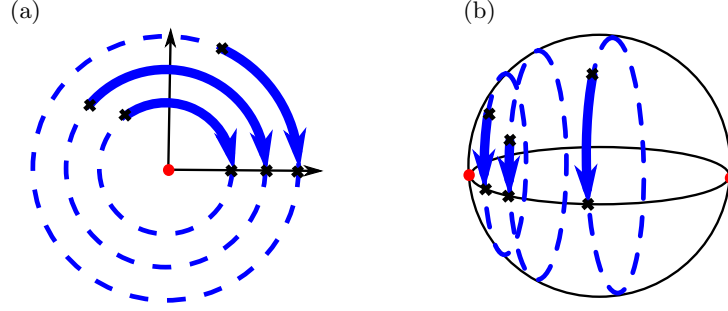


Fig. 6. Template shape estimation for the plane example (a) and the sphere example (b). The 3 black crosses in \mathbb{R}^2 (a) or S^2 (b) represent the 3 data. The 3 dotted blue curves are their orbits. The 3 curved blue arrows represent their registration, i.e. their projection in the shape space. The 3 black crosses in \mathbb{R}_+ (positive x-axis) (a) or $[0, \pi]$ (b) represent the registered data. The template shape estimate is the Fréchet mean of the registered data.

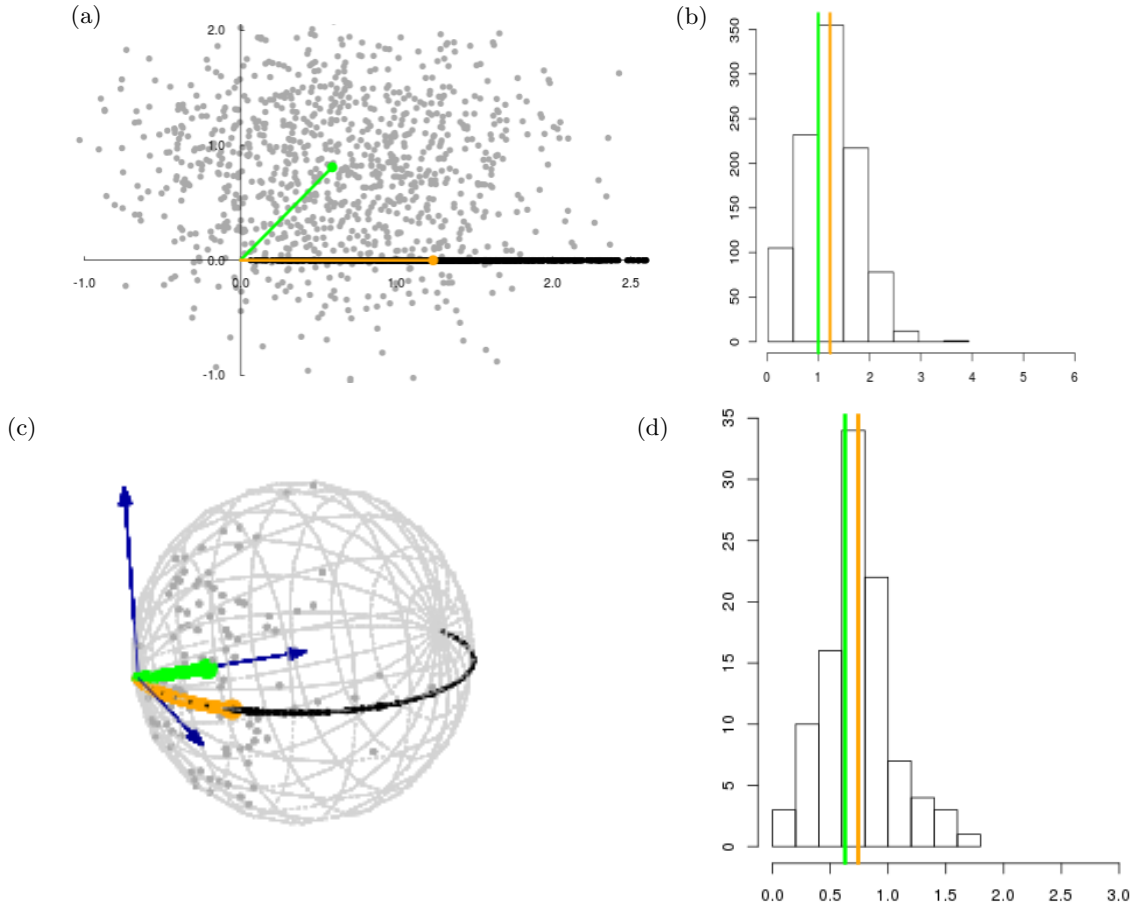


Fig. 7. Screenshot of <https://nmiolane.shinyapps.io/shinyPlane> and <https://nmiolane.shinyapps.io/shinySphere>. Simulated data (grey points), template shape (green), registered data (black points), template shape estimate (orange). Induced distributions on the shapes, template shape (green), template shape estimate (orange).

and <https://nmiolane.shinyapps.io/shinySphere>. We invite the reader to look at the web pages and play with the different parameters of the generative model. Figure 1.4 shows screen shots of the applications.

Our main result is to show that this procedure gives an inconsistent estimate of the template shape Y of the generative model. The estimator \hat{Y} converges when the number of data goes to infinity. However it has an asymptotic bias with respect to the parameter Y it is designed to estimate: $\text{Bias}(\hat{Y}, Y) = \text{mathbb{E}} \left[\text{Log}_Y \hat{Y} \right]$. This is a vector at the tangent space of M/G at the real parameter Y . The vector represents how much one has to shoot from Y to get the estimated parameter \hat{Y} . It simply writes $\text{Bias}(\hat{Y}, Y) = \mathbb{E} \left[\hat{Y} - Y \right]$ for linear spaces.

We could also consider the variance of the estimator. The variance is defined as $\text{Var}_n(\hat{Y}) = \mathbb{E}[d_M(Y, E[Y])^2]$. In the limit of an infinite sample, we have: $\text{Var}_\infty(\hat{Y}) = 0$. This is why we focus on the asymptotic bias.

2 Quantification and correction of the asymptotic bias

2.1 Asymptotic bias of the template's estimator on examples

We first compute the asymptotic bias for the examples of the plane and the sphere to give the intuition.

The probability distribution function of the X_i 's comes from the generative model. This is a probability distribution on \mathbb{R}^2 for the plane example, parameterized in polar coordinates (r, θ) like Figure 1. So we can compute the projected distribution function on the shapes, which are the radii r here. This is done simply by integrating out the distribution on θ , the position on the circles. This gives a probability distribution on \mathbb{R}_+ for the plane example. We write it $f : r \mapsto f(r)$. We remark that f does not depend on the probability distribution function on the θ_i 's of Step 2 of the generative model. We can also compute $f : \theta \mapsto f(\theta)$ in the sphere example: we integrate over ϕ the probability distribution function on (θ, ϕ) .

Figure 8 (a) shows f for the plane example, for a template $r = 1$. We plot it for two different noise levels $\sigma = 0.3$ and $\sigma = 3$. Note that here f is the Rice distribution. Figure 8 (b) shows f for the sphere example, for a template $\theta = 1$. We plot it for different noise levels and $\sigma = 0.3$ and $\sigma = 3$. In both cases, the x-axis represents the shape space which is \mathbb{R}_+ for the plane example and $[0, \pi]$ for the sphere example. The green vertical bar represents the template shape, which is 1 in both cases. The red vertical bar is the expectation of f in each case. It is \hat{Y} , the estimate of Y . We see on these plots that f is not centered at the template shape: the green and red bars do not coincide. f is skewed away from 0 in the plane example and away from 0 and π in the sphere example. The skew increases with the noise level σ . The difference between the green and red bars is precisely the bias of \hat{Y} with respect to Y .

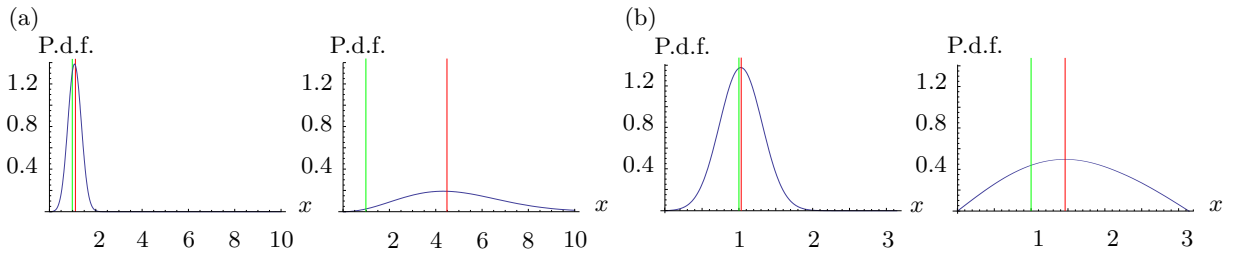


Fig. 8. (a) Induced distributions on the distance r between two landmarks in \mathbb{R}^3 for real distance $y = 1$ (in green) and noise level $\sigma = 0.3$ and $\sigma = 3$. (b) Induced distributions on the angle x between the two landmarks on S^3 , for real angle $y = 1$ and noise levels $\sigma = 0.3$ and $\sigma = 3$. In both cases the mean shape estimate \hat{y} is shown in red.

Figure 9 shows the bias of \hat{Y} with respect to Y , as a function of σ , for the plane (left) and the sphere (right). Increasing the noise level σ takes the estimate \hat{Y} away from Y . The estimate is

repulsed from 0 in the plane example: it goes to ∞ when $\sigma \rightarrow \infty$. It is repulsed from 0 and π in the sphere example: it goes to $\pi/2$ when $\sigma \rightarrow \pi$. One can show numerically that the bias varies as σ^2 around $\sigma = 0$ in both cases. This is also observed on the shiny applications [30] at <https://nmiolane.shinyapps.io/shinyPlane> and <https://nmiolane.shinyapps.io/shinySphere>.

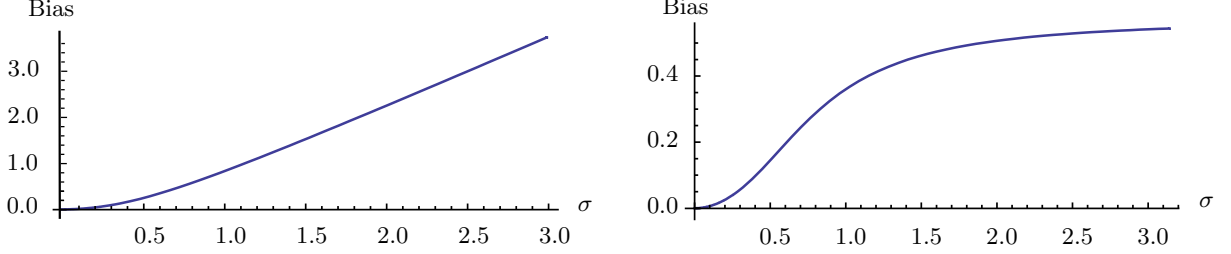


Fig. 9. Asymptotic bias on the mean shape estimate \hat{Y} with respect to the noise level σ for $r = 1$ in the plane example (a) and $\theta = 1$ in the sphere example (b). The bias is quadratic near $\sigma = 0$. Increasing σ takes the estimate \hat{Y} away from 0 in shape space $Q = \mathbb{R}_+$ (a) and away from 0 and π in shape space $Q = [0, \pi]$ (b).

These examples already show the origin of the asymptotic bias of \hat{Y} . *The bias comes from the curvature of the template's orbit.* Figure 10 shows the template's orbit in blue, in (a) for the plane and (b) for the sphere. In both cases the black circle represents the level set σ of the Gaussian noise. The probability of generating an observation X_i outside of the template's shape orbit is bigger than the probability of generating it inside: the grey area in the black circle is bigger than the white area in the white circle. There will be more registered data that are greater than the template. Their expected will therefore be greater than the template and thus biased. We prove this in the general case in the next section.

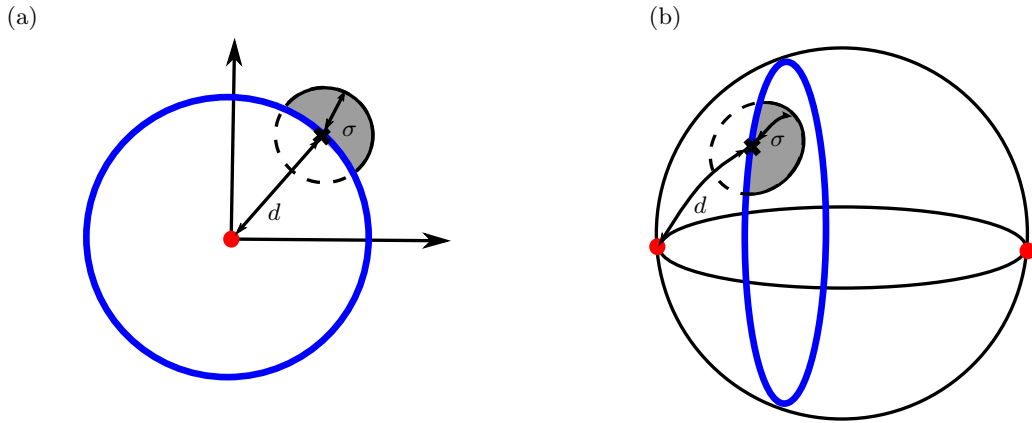


Fig. 10. The external curvature of the template's orbit creates the asymptotic bias, in the plane example (a) and the sphere example (b). The blue curve represents the template's orbit. The ball of radius σ represents a level set of the Gaussian distribution of the noise in \mathbb{R}^2 (a) and S^2 (b). The grey-colored area represents the distribution of the noise that generates data outside the orbit of Y . There is a higher probability that the data are generated "outside" the orbit. The template shape estimate is biased towards greater radii (a) or towards angles closer to $\pi/2$ (b).

2.2 Asymptotic bias of the template's estimator for the general case

We show the asymptotic bias of \hat{Y} in the general case and prove that it comes from the external curvature of the template's orbit. We show it for Y a principal shape and for a Gaussian noise of variance σ^2 , truncated at 3σ . Our results will need the following definitions of curvature.

The *second fundamental form* h of a submanifold O of M is defined on $T_X O \times T_X O$ by $h(v, w) = (\nabla_v w)^\perp \in N_X O$, where $(\nabla_v w)^\perp$ denotes the orthogonal projection of covariant derivative $\nabla_v w$ onto the normal bundle. The *mean curvature vector* H of O is defined as: $H = \text{Tr}(h)$. Intuitively, h and H are measures of extrinsic curvature of O in M . For example an hypersphere of radius R in \mathbb{R}^m has mean curvature vector $\|H\| = \frac{m-1}{R}$.

Theorem 1. *The probability distribution function on the shapes induced by the generative model is:*

$$f(x) = \frac{1}{c_q \sigma^q} \exp\left(-\frac{x^T x}{2\sigma^2}\right) \left(c_p^0 + c_p \sum_{ij} \left(\delta_{ij} - \frac{1}{6} R_{ij}^O - \sum_a \frac{1}{2} h_{ij}^a(x) x_a \right) \sigma^2 + \mathcal{O}(\sigma^4) \right).$$

Here x is the Riemannian logarithm $x = \text{Log}_Y[X]$ of the shape $[X]$ at the template shape Y , h is the second fundamental form of the orbit of x , R is the Ricci curvature, c_q, c_p, c_p^0 are constants independent of x and σ .

Proof. The proof is given in Appendix A.2. □

The exponential in the expression of f belongs to a Gaussian distribution centered at $x = 0$. This is a Riemannian Gaussian centered at the template shape Y , because x are coordinates at the tangent space of M/G at Y . However the whole distribution f differs from the Gaussian because of the x -dependent term in the right parenthesis. This induces a skew of the distribution away from the singular shapes, as observed for the examples in Figure 8.

Theorem 2. *The asymptotic bias of the template's shape estimation writes:*

$$\text{Bias}(\hat{Y}, Y) = \frac{\sigma^2}{2} H(Y) + \mathcal{O}(\sigma^3). \quad (3)$$

Here H is the mean curvature vector of the template shape's orbit and σ^2 the variance of the noise on the objects.

Proof. The proof is given in Appendix A.3. □

This generalizes the quadratic behavior observed in the examples on Figure 9. The asymptotic bias has a geometric origin: it comes from the external curvature of the template's orbits, see Figure 10.

We can vary two parameters in equation 3: Y and σ . The external curvature of orbits generally increases when Y is closer to a singularity of the shape space (see Section 1) [23]. The singular shape of the two landmarks in \mathbb{R}^2 arises when their distance is 0. In this case, the mean curvature vector is $H(Y) = \frac{1}{d}$: it is inversely proportional to d , the radius of the orbit. d is also the distance of Y to the singularity 0.

2.3 Limitations and extensions

Beyond Y being a principal shape Our results are valid when the template Y is a principal shape. This is a reasonable assumption as the set of principal shapes is dense in the shape space. What happens when Y approaches a singularity, i.e. when Y changes stratum in the stratified space Q ? Taking the limit $d \rightarrow 0$ in the coefficients of the Taylor expansion is not a legal operation. Therefore, we cannot conclude on the Taylor expansion of the Bias for $d \rightarrow 0$. Indeed, the Taylor expansion may even change order for $d \rightarrow 0$. We take $M = \mathbb{R}^m$ with the action of $SO(m)$ and the template $Y = (0, \dots, 0)$:

$$\text{Bias}(\hat{Y}, Y) = \sqrt{2} \frac{\Gamma(\frac{m+1}{2})}{\Gamma(\frac{m}{2})} \sigma. \quad (4)$$

The bias is linear in σ in this case.

Beyond $\sigma \ll 1$ The assumption $\sigma \ll 1$ is reasonable as we hope that the noise on the data is not too large. Nevertheless it would be very interesting to study the asymptotic bias for any σ , including large noises ($\sigma \rightarrow +\infty$). The distribution over the X_i 's in M will be spread on the whole manifold M . We cannot rely on local computations on M (at the scale of σ) anymore. We have to make global assumptions on the manifold M .

The plane example is the canonical example of a flat manifold. The sphere example is the canonical example of manifold with constant (positive) curvature. The bias as a function of σ is plotted in Figure 9. It leads us to the conjecture that the estimate converges towards a barycenter of shape space's singularities when the noise level increases. Singularities have a repulsive action on the estimation of each template's shape. Such repulsive force acts on each estimators. As a result, the estimators of the mean shape finds an equilibrium position: the barycenter.

Beyond one Dirac in Q : several templates We have considered so far that there is a unique template shape Y : the generative model has a Dirac distribution at Y in the shape space. What happens for other distributions? We assume that there are K template shapes Y_1, \dots, Y_K . Observations are generated in M from each template shape Y_k with the generative model of Section 2. Our goal is to unveil the structure of the shape distribution, i.e. the K template shapes here, given the observations in M . The distributions on shapes projected on the shape space is a mixture of probability density functions of the form of equation ???. Its modes are related to the template shapes. The K-means algorithm is a very popular method for data clustering. We study what happens if one uses K-means algorithms on shapes generated with the generative model above.

The goal is to cluster the shape data in K distinct and significant groups. One performs a coordinate descent algorithm on the following function:

$$J(c, \mu) = \sum_i d_Q(X_i, \mu_{c_i})^2. \quad (5)$$

In other words, one minimizes J by successively minimizing on the assignment labels c 's and the cluster's centers μ 's. Given the c , minimizing J with respect to the μ 's is exactly the simultaneous computation of K Fréchet means in the shape space. One looks for meaningful well separated clusters (high inter-clusters dissimilarity) whose members are close to each other (high intra-cluster similarity). In other words, the quality of the clustering is evaluated by the following criterion:

$$D = \min_{\text{clusters } i,j} \frac{d_Q(c_i, c_j)}{\max_i \text{diam}(c_i)}, \quad (6)$$

which is the dissimilarity between clusters quotiented by the diameter of the clusters. In the absence of singularity in the shape space, the projected distribution looks like Figure 11 (a) and $D \propto \frac{1}{\sigma}$. The criterion is worse in the presence of singularities.

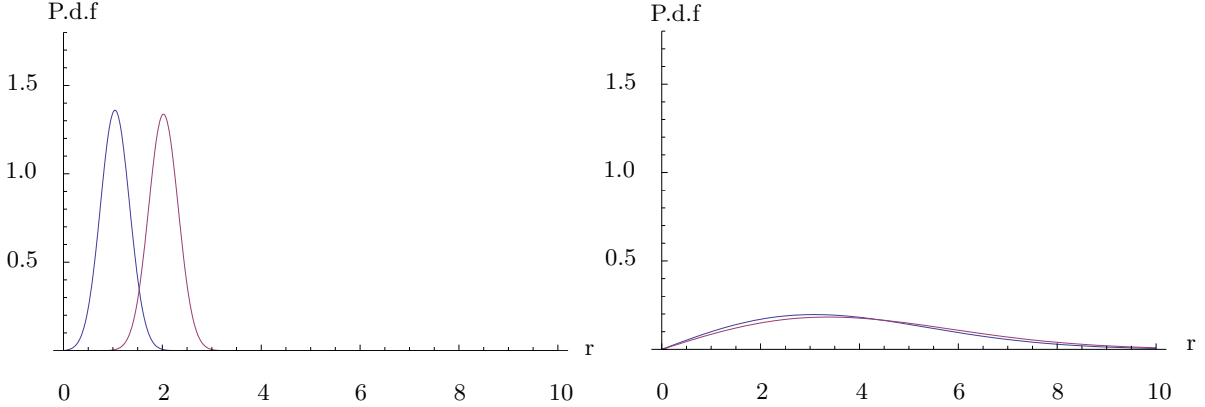


Fig. 11. Two clusters of template shapes for the plane example: $r_1 = 1$ (blue) and $r_2 = 2$ (dark red). Noise levels: $\sigma = 0.3$ (left) and $\sigma = 3$ (right). The 2 clusters are hardly distinguishable when the noise increases.

Figure 11 illustrates this behavior for the plane example. We consider any two clusters i, j and call \hat{Y}_i, \hat{Y}_j the estimated centroids. The criterion D writes:

$$D \equiv \frac{\hat{y}_i - \hat{y}_j}{\sigma} \underset{\sigma \rightarrow +\infty}{\sim} \frac{\Gamma\left(\frac{m+1}{2}\right)}{\sqrt{2}m\Gamma\left(\frac{m}{2}\right)} \frac{y_i^2 - y_j^2}{\sigma^2} = O\left(\frac{1}{\sigma^2}\right).$$

Even in the best case with correct assignments to the clusters i and j , the K-means algorithm looses an order of validation when computed on shapes.

Beyond the finite dimensional case Our results are valid when M is a finite dimensional manifold and G a finite dimensional Lie group. Some interesting examples belong to the framework of infinite dimensional manifold with infinite dimensional Lie groups. This is the case for the LDDMM framework on images [15]. It would be important to extend these results to the infinite dimensional case.

We take $M = \mathbb{R}^m$ with the action of $SO(m)$. We have a analytic expression of f in this case [24]. Figure 12 shows the influence of the dimension m for the probability distribution functions on the shape space and for the Bias. The bias increases with m . This leads to think that it appears in infinite dimensions as well.

3 Correction of the systematic bias

We propose two procedures to correct the asymptotic bias on the template's estimate. They rely on the bootstrap principle [11], more precisely a parametric bootstrap. As such, they are directly applicable to any type of data. We assume that we know the variance $\hat{\sigma}^2$ from the experimental setting.

3.1 Iterative Bootstrap

The first procedure is called Iterative Bootstrap. Algorithm 3.1 details it. Figure 13 illustrates it on the plane example.

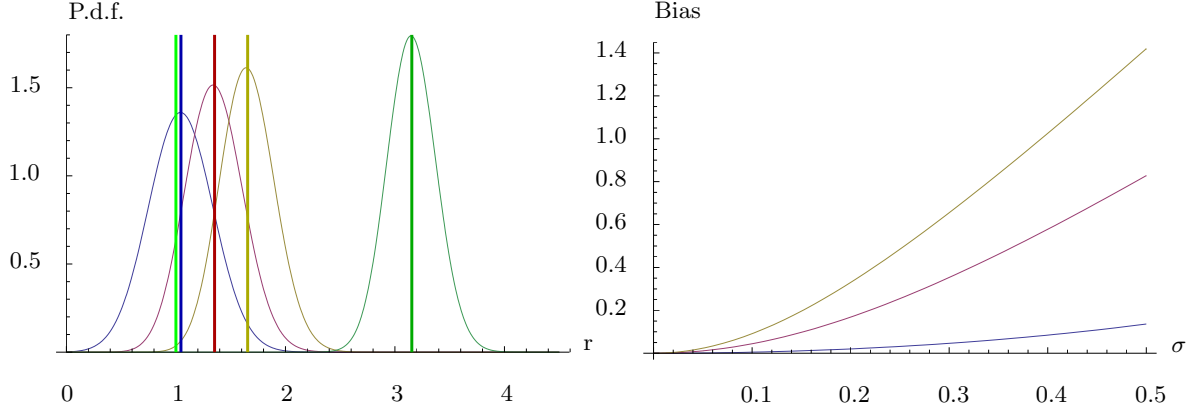


Fig. 12. Probability distributions functions (noise $\sigma = 0.3$) and bias for \mathbb{R}^m for $m = 2$, $m = 10$, $m = 20$ and $m = 100$. Template shape is $r = 1$.

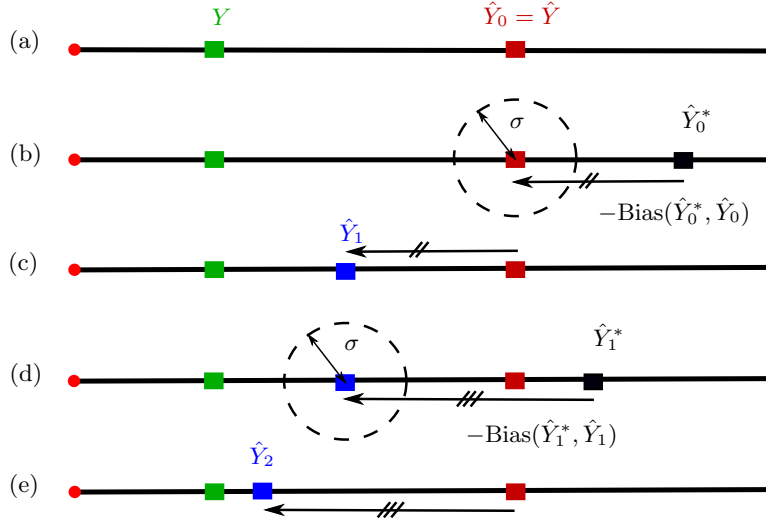


Fig. 13. Algorithm 3.1 Iterative bootstrap procedure on the plane example for $n \rightarrow +\infty$. (a) Initialization, (b) Generate bootstrap sample from \hat{Y}_0 and compute the corresponding estimate \hat{Y}_0^* , compute the bias $\hat{Y}_0 - \hat{Y}_0^*$, (c) Correct \hat{Y}_0 with the bias to get \hat{Y}_1 , (d) Generate bootstrap sample from \hat{Y}_1 and iterate as in (b), (e) Get \hat{Y}_2 etc.

Algorithm 3.1 starts with the usual template's estimate $\hat{Y}_0 = \hat{Y}$, see Figure 13 (a). At each iteration, we correct \hat{Y} with a better approximation of the bias. First, we generate bootstrap data by using \hat{Y} as the template shape of the generative model. We perform the template's estimation procedure with the Fréchet mean in the shape space. This gives an estimate \hat{Y}_0^* of \hat{Y}_0 . The bias of \hat{Y}_0^* with respect to \hat{Y}_0 is $\text{Bias}(\hat{Y}_0^*, \hat{Y}_0)$. It gives an approximation of the bias $\text{Bias}(\hat{Y}, \hat{Y})$, see Figure 13 (b). We correct \hat{Y} by this approximation of the bias. This gives a new estimate \hat{Y}_1 , see Figure 13 (c). We recall that the bias $\text{Bias}(\hat{Y}, \hat{Y})$ depends on Y , see Theorem 2. \hat{Y}_1 is closer to the template Y than \hat{Y}_0 . Thus, the next iteration gives a better approximation $\text{Bias}(\hat{Y}_1^*, \hat{Y}_1)$ of $\text{Bias}(\hat{Y}, \hat{Y})$. We correct the initial \hat{Y} with this better approximation of the bias, etc. The procedure is written formally for a general manifold M in Algorithm 3.1.

In Algorithm 3.1, Π_A^B denotes the parallel transport from $T_A M$ to $T_B M$. For linear spaces, $\text{Log}_{P_1} P_2 = \overrightarrow{P_1 P_2}$, $\text{Exp}_{P_1}(u) = P_1 + u$, $\Pi_{P_1}^{P_2}(u) = u$.

Algorithm 1 Corrected template shape estimation with **Iterative Bootstrap**

Input: Objects $\{X_i\}_{i=1}^n$, noise variance σ^2

Initialization:

$\hat{Y}_0 = \text{Fréchet}(\{[X_i]\}_{i=1}^n)$

$k \leftarrow 0$

Repeat:

Generate bootstrap sample $\{X_i^{(k)*}\}_{i=1}^n$ from $\mathcal{N}_M(Y_k, \sigma^2)$

$\hat{Y}_k = \text{Fréchet}(\{[X_i^{(k)*}]\}_{i=1}^n)$

$\text{Bias}_k = \text{Log}_{Y_k} \hat{Y}_k$

$\hat{Y}_k = \text{Exp}_{\hat{Y}_0}(-\Pi_{\hat{Y}_k}^{\hat{Y}_0}(\text{Bias}_k))$

$k \leftarrow k + 1$

until convergence: $\|\text{Log}_{\hat{Y}_{k+1}} \hat{Y}_k\| < \epsilon$

Output: \hat{Y}_k

Algorithm 3.1 is a fixed-point iteration $Y^{(k+1)} = F(Y^{(k)})$ where:

$$F(X) = \text{Exp}_{\hat{Y}}(-\Pi_X^{\hat{Y}}(\text{Bias})) \quad \text{where:} \quad \text{Bias} = \text{Log}_X \hat{X}. \quad (7)$$

In a linear setting we have simply $F(X) = \hat{Y} - \overrightarrow{X\hat{X}}$. One can show that F is a contraction and that Y , the template shape, is the unique fixed point of F (using the local bijectivity of the Riemannian exponential and the injectivity of the estimation procedure). Thus the procedure converges to Y in the case of an infinite number of observations $n \rightarrow +\infty$. Figure 14 illustrates the convergence for the plane example, with a Gaussian noise of standard deviation $\sigma = 1$. The template shape $Y = 1.2$ was initially estimated at $\hat{Y} = 4.91$. Algorithm 3.1 corrects the bias.

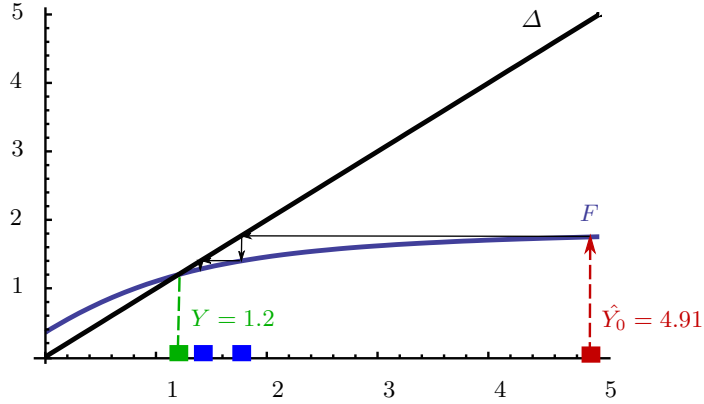


Fig. 14. F of the fixed-point procedure and first 2 iterations for $\sigma = 1$, $m = 3$. Δ is the first diagonal. The initial estimate is biased $\hat{Y}_0 = 4.91$. The Iterative Bootstrap converges towards the template shape $Y = 1.2$.

Figures 15 and 16 show the iterations of Iterative Bootstrap for the plane and the sphere example.

3.2 Nested Bootstrap

The second procedure is called the Nested Bootstrap. Algorithm 3.2 details it. Figure 17 illustrates it on the plane example.

Algorithm 3.2 starts like Algorithm 3.1 with $\hat{Y}_0 = \hat{Y}$, see Figure 17 (a). It also performs a parametric bootstrap with $\hat{Y}^{(0)}$ as the template, computes the bootstrap replication \hat{Y}_0^* and the

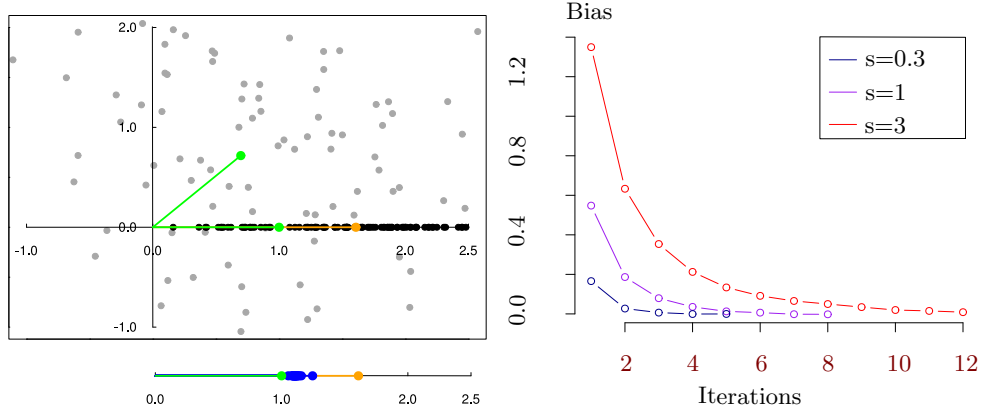


Fig. 15. Convergence of Algorithm 3.1, Iterative Bootstrap for the plane example. The different colors represent the variance of the noise.

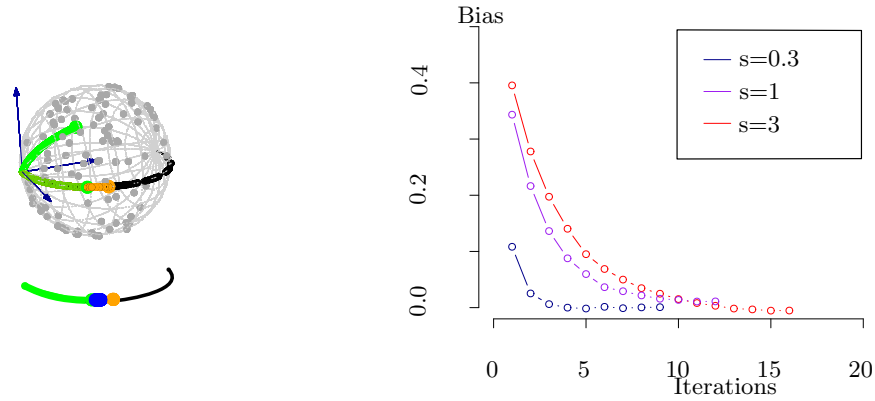


Fig. 16. Convergence of Algorithm 3.1, Iterative Bootstrap, for the sphere example. The different colors represent the variance of the noise.

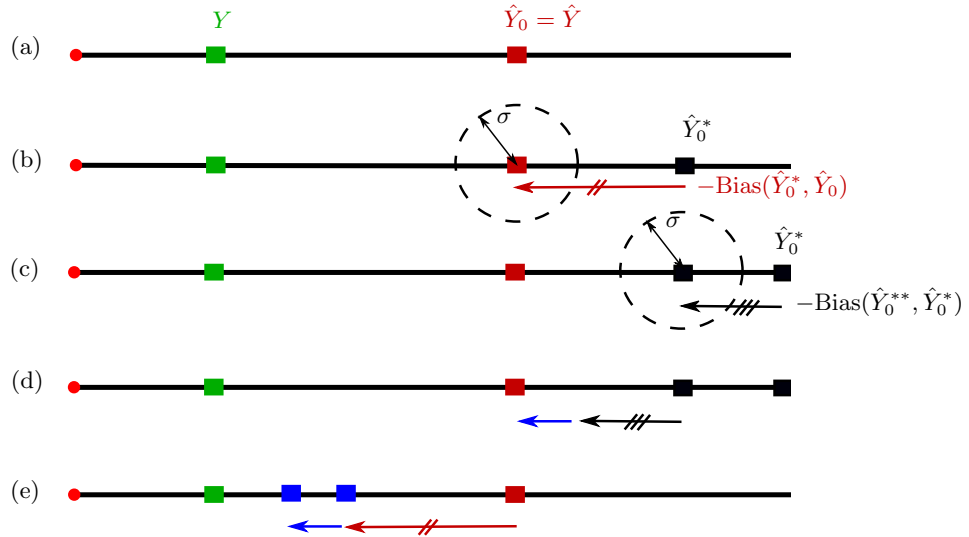


Fig. 17. Algorithm 3.2 Nested Bootstrap on the plane example for $n \rightarrow +\infty$. (a) Initialization, (b) Generate bootstrap sample from \hat{Y}_0 ; compute the estimate \hat{Y}_0^* , compute the bias $\hat{Y}_{(0)} - \hat{Y}_0^*$, (c) Generate bootstrap sample from \hat{Y}_0^* ; compute the estimate \hat{Y}_0^{**} , compute the bias $\hat{Y}_0^* - \hat{Y}_0^{**}$, (d) compute the blue arrow, i.e. the bias of $\text{Bias}(\hat{Y}_0^{**}, \hat{Y}_0^*)$ as an estimate of $\text{Bias}(\hat{Y}_0^*, \hat{Y}_0)$, (e) Correct \hat{Y} with the bias-corrected bias.

approximation $\text{Bias}(\hat{Y}_0^*, \hat{Y}_0)$ of $\text{Bias}(\hat{Y}, Y)$, see Figure 13 (b). Now Algorithm 3.2 differs from Algorithm 3.1. We want to know how biased is $\text{Bias}(\hat{Y}_0^*, \hat{Y}_0)$ as an estimate of $\text{Bias}(\hat{Y}, Y)$? This is a valid question as the bias depends on the template Y , see Theorem 2. We want to estimate this dependence. We perform a bootstrap, nested in the first one, with $\hat{Y}^{(0)*}$ as the template. We compute the estimate \hat{Y}_0^{**} and the approximation $\text{Bias}(\hat{Y}_0^{**}, \hat{Y}_0^*)$ of $\text{Bias}(\hat{Y}_0^*, \hat{Y}_0)$, see Figure 13 (c). We observe how far $\text{Bias}(\hat{Y}_0^{**}, \hat{Y}_0^*)$ is from $\text{Bias}(\hat{Y}_0^*, \hat{Y}_0)$. This gives the blue arrow, which is the bias of $\text{Bias}(\hat{Y}_0^{**}, \hat{Y}_0^*)$ as an estimate of $\text{Bias}(\hat{Y}_0^*, \hat{Y}_0)$, see Figure 13 (d). The blue arrow is an approximation of how far $\text{Bias}(\hat{Y}_0^*, \hat{Y}_0)$ is from $\text{Bias}(\hat{Y}, Y)$. We correct our estimation of the bias (in red) by the blue arrow. We correct \hat{Y} by the bias-corrected estimate of its bias, see Figure 13 (e).

Algorithm 2 Corrected template shape estimation with **Nested Bootstrap**

Input: Objects $\{X_i\}_{i=1}^n$, noise variance σ^2

Initialization:

$\hat{Y}_0 = \text{Frechet}(\{[X_i]\}_{i=1}^n)$

Bootstrap:

Generate bootstrap sample $\{X_i^*\}_{i=1}^n$ from $\mathcal{N}_M(\hat{Y}_0, \sigma^2)$

$\hat{Y}_0^* = \text{Fréchet}(\{[X^*]_i\}_{i=1}^n)$

$\text{Bias} = \text{Log}_{\hat{Y}_0^*} \hat{Y}_0^*$

Nested Bootstrap:

For each i :

- Generate bootstrap sample $\{X_i^{**}\}_{k=1}^n$ from $\mathcal{N}_M(\hat{Y}_0^*, \sigma^2)$
- $\hat{Y}_{0,i}^{**} = \text{Fréchet}(\{[X^{**}]_i\}_{k=1}^n)$

$\text{Bias}(\text{Bias}) = \text{Log}_{\hat{Y}_0^*} \hat{Y}_0^* - \Pi_{\hat{Y}_0^*}^{\hat{Y}_0} \text{Log}_{\hat{Y}_0^*} \hat{Y}_{0,i}^{**}$

$\hat{Y}_1 = \text{Exp}_{\hat{Y}_0^*}(-\text{Bias} - \text{Bias}(\text{Bias}))$

Output: \hat{Y}_1

3.3 Comparison

One may use the Iterative Bootstrap or the Nested Bootstrap depending on the experimental setting. We illustrate them both on the plane example in Figure 18.

The advantages of the Iterative Bootstrap are the following. It corrects perfectly the bias of \hat{Y} in the case of a very large number of observations n . It can be used to experimentally compute the mean curvature vector H of each orbit of a group action. One probes the orbit's curvature by "feeling it" with a Riemannian Gaussian on M and projecting on the shape space. Its drawbacks are the following. It works only with very large n . It is not robust as it uses the generative model several times. If the generative model is far from being true, then the iterative bootstrap fails.

The advantages of the Nested Bootstrap are the following. It is a standard statistical procedure that is more robust with respect to variations of the generative model. Even if generative model is different from the one that we assume, the Nested Bootstrap performs well. Moreover, it does not need as many data as the Iterative Bootstrap. Its drawback is that it does not correct perfectly the bias, especially when the noise is important.

These simulations give a rule of thumb for when the bias needs to be corrected. This is when the noise σ is comparable to the distance of the template Y to the singularity.

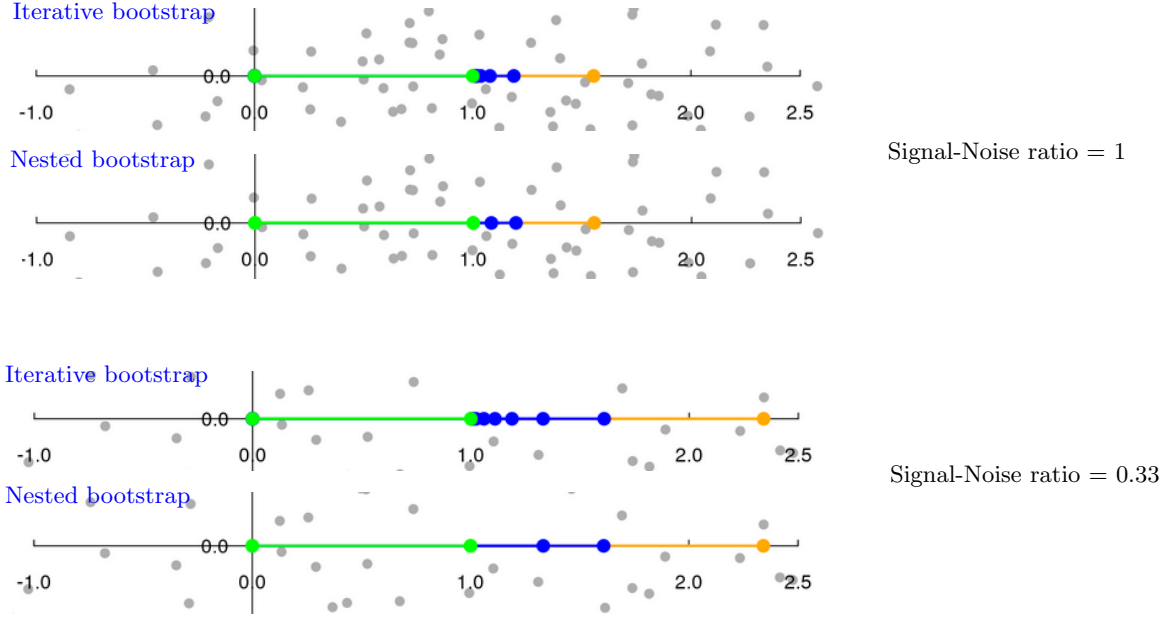


Fig. 18. Comparison of the Iterative bootstrap and the Nested bootstrap on simulation with two different Signal-Noise ratio, which is $\frac{Y}{\sigma}$, the ratio of the template Y on the noise level σ .

4 Applications to simulated and real data

4.1 Simulated triangles

We perform a simulation using the iterative bootstrap on triangles. We randomly generate $n = 10^5$ triangles in \mathbb{R}^2 . The mean triangle is chosen by taking two coordinates randomly from a uniform distribution on $[0, 1]$. Then we add bivariate Gaussian noise on each landmark. These experiments are illustrated in Figure 19.

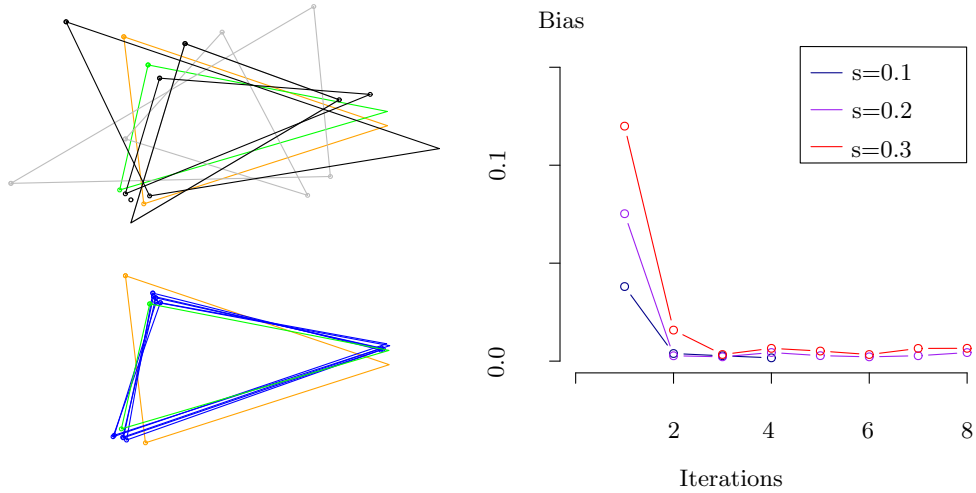


Fig. 19. Convergence of Algorithm 3.1, Iterative Bootstrap for the triangles. The different colors represent the variance of the noise.

The number of iterations required for the convergence of Algorithm 1 with respect to the noise level are shown in Figure 19. We observe the convergence in the three experiments for less than 10 iterations.

4.2 Real triangles: shape of the Optic Nerve Head

Now we go to real triangle data. We have 24 images of Rhesus monkeys' eyes, acquired with a Heidelberg Retina Tomograph [25]. For each monkey, an experimental glaucoma was introduced in one eye, while the second eye was kept as control. One seeks a significant difference between the glaucoma and the control eyes. On each image, three anatomical landmarks were recorded: S for the superior aspect of the retina, N for the nose side of the retina, and T for the side of the retina closest to the temporal bone of the skull. The data are matrices $\{X_i\}_{i=1}^n$ where the landmark coordinates form the rows. For the ONH example, M is the space of 3 landmarks in 3D, $M = (\mathbb{R}^3)^3$ and the rotations act isometrically on each object X_i .

Analysis This simple example illustrates the estimation of the template shape. We use the following procedure to compute the mean shape for each group. We initialize \hat{Y} with X_1 and repeat the following two steps until convergence:

- (1) $\forall i \in \{1, \dots, n\}, \quad \hat{R}_i = \operatorname{argmin}_{R \in SO(3)} \|\hat{Y} - X_i \cdot R\|^2, \quad (\text{register to the current mean shape}),$
- (2) $\hat{Y} = \frac{1}{n} \sum_{i=1}^n X_i \cdot \hat{R}_i \quad (\text{update the mean shape estimate}).$

Figure 20 shows the mean shapes \hat{Y}^{control} of the control group (left) and $\hat{Y}^{\text{glaucoma}}$ of the glaucoma group (right) in orange, while the initial data are in grey. The difference between the two groups is quantified by the distance between their means: $\|\hat{Y}^{\text{control}} - \hat{Y}^{\text{glaucoma}}\| = 21.84\mu\text{m}$. We want to determine if this analysis presents an bias that significantly changes the estimated shape difference between the groups.

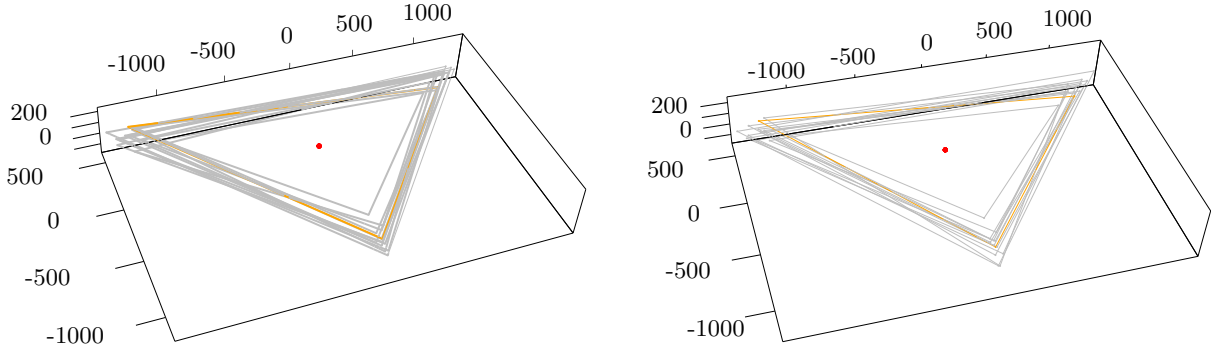


Fig. 20. Triangles data in grey for the control group (left) and the glaucoma group (right). In orange, the estimated template shapes. Distances are measured in μm .

We use the nested bootstrap to compute an approximation of the asymptotic bias on each mean shape, for a range of noise's standard deviation in $\{100\mu\text{m}, 200\mu\text{m}, 300\mu\text{m}, 400\mu\text{m}\}$. The asymptotic bias on the template shape of the glaucoma group is $\{0.1\mu\text{m}, 0.11\mu\text{m}, 0.12\mu\text{m}, 0.13\mu\text{m}\}$ and of the control group is $\{0.27\mu\text{m}, 0.42\mu\text{m}, 0.55\mu\text{m}, 0.67\mu\text{m}\}$. The corrected template shape differences are $\{22.01\mu\text{m}, 22.08\mu\text{m}, 22.14\mu\text{m}, 22.18\mu\text{m}\}$. In particular, for $\sigma = 400\mu\text{m}$, we observe that the bias in the template shape are respectively $0.67\mu\text{m}$ for the healthy group and $0.13\mu\text{m}$ for the glaucoma group. This follows the rule-of-thumb: the bias is more important for

the healthy group, for which the overall size is smaller than the glaucoma group, for a same noise level. The bias of the template shape estimate accounts for less than $1\mu\text{m}$ in this case, which is less than 0.1% of the shapes' sizes. This computation guarantees that this study has not been significantly affected by the bias.

4.3 Protein shapes in Molecular Biology

We estimate the impact of the bias on statistics on protein shapes.

A standard hypothesis in Biology is that structure (i.e. shape) and function of proteins are related. Fundamental research questions about protein shapes include structure prediction - given the protein amino-acid sequence, one tries to predict its structure - and design - given the shape, one tries to predict the sequence needed.

One relies on experimentally determined 3D structures gathered in the Protein Data Base (PDB) [5]. They contain errors on the protein's atoms coordinates. Average errors range from 0.01 Å to 1.76 Å, which is of the magnitude of the length of some covalent bonds. These values are averaged over the whole protein and in general, the main-chain atoms are better defined than the side-chain atoms or the atoms at the periphery. This is illustrated on Figure where we have plot the B-factor (related to coordinates errors [31]) as a colored map on the atoms for proteins of PDB-codes 1H7W and 4HBB.

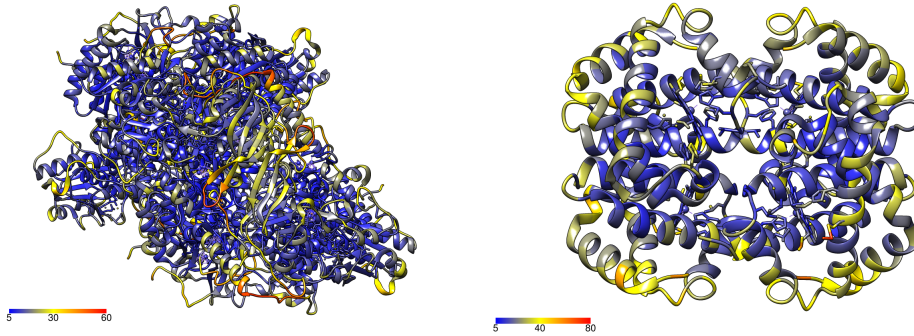


Fig. 21. Errors on atoms coordinates represented by the B-factor, for proteins 1H7W (left) and 4HBB (right). Atoms at the periphery of the proteins tend to have more errors, which appear in yellow-red colors.

Protein's radius of gyration A biased estimate of a protein shape has consequences for studies on proteins folding. Stability and folding speed of a protein depend on both the estimated shape of the denatured state (unfolded state) and of the native state (folded state). One may study if compact initial states yield to faster folding. The protein compactness is represented by the protein's Radius of Gyration, defined as: $R_g^2 = \frac{1}{N} \sum_{\text{non H atoms } i} (r_i - R_C)^2$, where N is the number of non-hydrogen atoms, r_i , R_C are resp. the coordinates of atoms and centers and m_i their mass. Note that we assume (as it is usually the case) that all masses m_i for non-hydrogen atoms are equal and that hydrogen atoms have mass 0. Error on atoms coordinates give a bias on the estimate of the Radius of Gyration:

$$\mathbb{B}(R_g^2) = \bar{R}_g^2 \frac{(N-1)}{N} \frac{3}{2\alpha^2}. \quad (8)$$

The radius of protein HJSJ (85 residues) is known to be around 10 Å. The error on R_g^2 is of 0.3% with an average error of positions on the atoms of 0.3Å. It is 8.6% for an error of 1.7Å.

The error will be greater if one consider binding sites at the periphery of the proteins rather than the whole protein. Indeed sites' size is smaller and they have less atoms.

One could think about doing clustering on radii of Gyration using the K-means algorithm on shapes. The index D of Section 3 is:

$$D = \frac{R_1^{\sigma^2} - R_2^{\sigma^2}}{\sigma} = \frac{R_1^2 - R_2^2}{\sigma} + 3\sigma \left(\frac{N_1 - 1}{N_1} - \frac{N_2 - 1}{N_2} \right). \quad (9)$$

Clustering on radii of gyration may lead to a misleading indicator. D indicates that the clustering performs better than it actually does.

False positive probability in protein's motif detection The relation between a protein's shape and function is linked to its motifs, which define the supersecondary structure. Motifs have biological properties: for example the helix-turn-helix motif [8] is responsible for the binding of DNA within several prokaryotic proteins. Automatic motif detection is another challenge in the study of protein shapes. We investigate the impact of bias on the false positive probability estimation in motif detection.

Let us consider a set $\{P_i\}_{i=1}^n$ of proteins each with N_i atoms. One is interested in the motifs of k atoms that can be detected in the protein's set, where $k < N$. We define σ that represents an allowed error zone. The number of detected motifs increases if: (i) one decreases k , or (ii) one increases σ , or (iii) increases n . Thus how many detected motifs actually come from chance, with respect to the parameters k , σ , n ? The false positives probability indicates when one detects truth and when one detects noise. The usual estimate of the false positive probability is $P = \frac{\mathcal{V}_0}{\mathcal{V}_l}$. Here \mathcal{V}_0 is the volume of the error zone allowed. \mathcal{V}_l is the total volume of the protein [26], thus the a ball of radius the Radius of Gyration. Thus \mathcal{V}_l may be biased and overestimated. The probability of false positive is underestimated.

We consider the example of [28]. One tries to find motifs between the tryptophan repressor of Escherichia coli (PDB code 2WRP) and the CRO protein of phage 434 (PDB code 2CRO). These two proteins are known to share the helix-turn-helix motif. The radius of Gyration of 2WRP is $R_g = 20\text{\AA}$, the total volume is: $\mathcal{V}_l = \frac{4}{3}\pi R_g^3 \simeq 33510\text{\AA}^3$. We assume an error zone that takes the form of a diagonal covariance matrix with standard deviations $\sigma = 0.35\text{\AA}$. We get the error zone volume: $\mathcal{V}_0 = \chi^{\frac{3}{2}} \pi \sigma^3 = 4.06\text{\AA}^3$ and the estimation of the false positive probability: $P = 1.2 \times 10^{-4}$. We find that P is underestimated by 0.27% using the expression of the Radius of Gyration's bias.

4.4 Brain template in Neuroimaging

We apply the rule of thumb of Section 3 to determine when the bias needs a correction in the computation of a brain template from medical images. Here M and G will be infinite dimensional. Nevertheless we apply our results to get intuition for this application.

In neuroimaging, a template is an image representing a reference anatomy. Computing the template is often the first step in medical image processing. Then, the subjects' anatomical shapes may be characterized by their spatial deformations *from the template*. These deformations may serve for (i) a statistical analysis of the subject shapes, or (ii) for automated segmentation by mapping the template's segmented regions into the subject spaces. In both cases, if the template is not centered among the population, i.e. if it is biased, then the analyzes and conclusions could be biased. We are interested in highlighting the variables that control the template's bias.

The framework of Large Deformation Diffeomorphic Metric Mapping (LDDMM) [32] embeds the template estimation in our geometric setting. The Lie group of diffeomorphisms acts on the

space of images as follows:

$$\rho : \text{Diff}(\Omega) \times L_2(\Omega) \rightarrow L_2(\Omega), \quad (\phi, I) \mapsto \phi \cdot I = I \circ \phi^{-1}. \quad (10)$$

The isotropy group of I writes: $G_I = \{\phi \in \text{Diff}(\Omega) | I \circ \phi^{-1} = I\}$. Its Lie algebra \mathfrak{g}_I consists of the infinitesimal transformations whose vector fields are parallel to the level sets of I : $\mathfrak{g}_I = \{v | \forall x \in \Omega, \nabla I(x)^T \cdot v(x) = 0\}$. The orbit of I is : $O_I = \{I' \in L_2(\Omega) | \exists \phi \in \text{Diff}(\Omega) \text{ s.t. } I' \circ \phi^{-1} = I\}$.

The "shape space" is by definition the space of orbits. Two images that are diffeomorphic deformations of one another are in the same orbit. They correspond to the same point in the shape space. Topology of an image is defined as the image's properties that are invariant by diffeomorphisms. Consequently, the shape space is the space of the images topology, represented by the topology of their level sets. We get a stratification of the shape space when we gather the orbits by orbit type. A stratum is more singular than another, if it has higher orbit type, i.e. larger isotropy group.

The manifold M has an infinite stratification. One changes stratum every time there is a change in the topology of an image's level sets. Singular strata are toward simpler topology. "Principal" strata are toward a more complicated topology. Indeed, the simpler the topology of the level sets is, the higher is the "symmetry" of the image. Thus the larger is its isotropy group. Note that strata with smaller isotropy group (more detailed topology) do not represent "singularities" from the point of view of a given image and do not influence the bias. In fact, such strata are at distance 0: an infinitesimal local change in intensity can create a maximum or minimum, thus complexifying the topology.

Using the rule-of-thumb of Section 3, the template's bias depends on its distance d to the next singularity, at the scale of σ the intersubjects variability. The template is biased in the regions where the difference in intensity between maxima and minima is of the same amplitude as the variability. The template may converge to pure noise in these regions.

Conclusion

We introduced tools of statistics on manifolds to study the properties of template's shape estimation in Medical imaging and Computer vision. We have shown its asymptotic bias by considering the shape space's geometry. The bias comes from the external curvature of the template's orbit at the scale of the noise on the data. This provides a geometric interpretation for the bias observed in [2,3]. We investigated the case of several templates and the performance K-mean algorithms on shapes: clusters are less well separated because of each centroid's bias. The variables controlling the bias are: (i) the distance in shape space from the template to a singular shape and (ii) the noise's scale. This gives a rule-of-thumb for determining when the bias is important and needs correction. We proposed two procedures for correcting the bias: an iterative bootstrap and a nested bootstrap. These procedures can be applied to any type of shape data: landmarks, curves, images, etc. They also provide a way to compute the external curvature of an orbit.

Our results are exemplified on simulated and real data. Many studies use the template's shape estimation algorithm in Molecular Biology, Medical Imaging or Computer vision. Their estimations are necessarily biased. But these studies often belong to a regime where the bias is not important (less than 0.1%). For example, the bias is important in landmark shapes analyses when the landmarks' noise is comparable to the template shape's size. Studies are rarely in this regime. We have considered shapes belonging to infinite dimensional shape spaces. Our results do not apply to the infinite dimensional case. We have used them to gain intuition about it. The bias might be more important in infinite dimensions and need the correction we have suggested.

References

1. D. ALEKSEEVSKY, A. KRIEGL, M. LOSIK, AND P. W. MICHOR, *The Riemannian geometry of orbit spaces. the metric, geodesics, and integrable systems*, Publ. Math. Debrecen, 62 (2003).
2. S. ALLASSONNIÈRE, Y. AMIT, AND A. TROUVÉ, *Towards a coherent statistical framework for dense deformable template estimation*, Journal of the Royal Statistical Society., 69 (2007), pp. 3–29.
3. S. ALLASSONNIÈRE, L. DEVILLIERS, AND X. PENNEC, *Estimating the template in the total space with the Fréchet mean on quotient spaces may have a bias.*, Proceedings of the fifth international workshop on Mathematical Foundations of Computational Anatomy (MFCA’15), 2015, pp. 131–142.
4. S. ALLASSONNIÈRE AND E. KUHN, *Convergent stochastic expectation maximization algorithm with efficient sampling in high dimension. application to deformable template model estimation*, Computational Statistics & Data Analysis, 91 (2015), pp. 4 – 19.
5. H. M. BERMAN, J. WESTBROOK, Z. FENG, G. GILLILAND, T. N. BHAT, H. WEISSIG, I. N. SHINDYALOV, AND P. E. BOURNE, *The protein data bank*, Nucleic Acids Res, 28 (2000), pp. 235–242.
6. J. BIGOT AND B. CHARLIER, *On the consistency of Fréchet means in deformable models for curve and image analysis*, Electronic Journal of Statistics, (2011), pp. 1054–1089.
7. J. BIGOT AND S. GADAT, *A deconvolution approach to estimation of a common shape in a shifted curves model*, Ann. Statist., 38 (2010), pp. 2422–2464.
8. R. G. BRENNAN AND B. W. MATTHEWS, *The helix-turn-helix dna binding motif.*, Journal of Biological Chemistry, 264 (1989), pp. 1903–6.
9. H. DARMANT, B. BUGNAS, R. B. D. DOMPSURE, L. BARRESI, N. MIOLANE, X. PENNEC, F. DE PERETTI, AND N. BRONSARD, *Analyse biométrique de lanneau pelvien en 3 dimensions propos de 100 scanners*, Revue de Chirurgie Orthopédique et Traumatologique, 100 (2014), pp. S241 –.
10. I. DRYDEN AND K. MARDIA, *Statistical shape analysis*, John Wiley & Sons, New York, 1998.
11. B. EFRON, *Bootstrap methods: Another look at the jackknife*, The Annals of Statistics, 7 (1979), pp. 1–26.
12. A. M. T. ELEWA, *Morphometrics for Nonmorphometricians*, Springer, 2012.
13. A. EVANS, A. JANKE, D. COLLINS, AND S. BAILLET, *Brain templates and atlases*, Neuroimage, 62(2) (2012), pp. 911–922.
14. S. HUCKEMANN, T. HOTZ, AND A. MUNK, *Intrinsic shape analysis: Geodesic principal component analysis for riemannian manifolds modulo lie group actions.*, Statistica Sinica, 20 (2010), pp. 1–100.
15. S. JOSHI, D. KAZISKA, A. SRIVASTAVA, AND W. MIO, *Riemannian structures on shape spaces: A framework for statistical inferences*, in Statistics and Analysis of Shapes, 2006, pp. 313–333.
16. D. G. KENDALL, *The diffusion of shape*, Advances in applied probability, 9 (1977), pp. 428–430.
17. D. G. KENDALL, *Shape manifolds, Procrustean metrics, and complex projective spaces*, Bulletin of the London Mathematical Society, 16 (1984), pp. 81–121.
18. S. A. KURTEK, A. SRIVASTAVA, AND W. WU, *Signal estimation under random time-warps and nonlinear signal alignment*, in Advances in Neural Information Processing Systems 24, 2011, pp. 675–683.
19. H. LE AND D. G. KENDALL, *The riemannian structure of euclidean shape spaces: A novel environment for statistics*, The Annals of Statistics, 21 (1993), pp. 1225–1271.
20. S. LELE, *Euclidean distance matrix analysis (EDMA): estimation of mean form and mean form difference*, Mathematical Geology, 25 (1993), pp. 573–602.
21. J.-Y. LI, E. ENGLUND, J. HOLTON, D. SOULET, P. HAGELL, A. LEES, T. LASHLEY, N. QUINN, S. REHNCRONA, A. BJORKLUND, H. WIDNER, T. REVESZ, O. LINDVALL, AND P. J. . BRUNDIN.
22. M. LORENZI, N. AYACHE, G. B. FRISONI, AND X. PENNEC, *Mapping the effects of $A\beta_{1-42}$ levels on the longitudinal changes in healthy aging: hierarchical modeling based on stationary velocity fields*, in Proceedings of Medical Image Computing and Computer Assisted Intervention (MICCAI), vol. 6892 of LNCS, Springer, 2011, pp. 663–670.
23. A. LYTCHAK AND G. THORBERGSSON, *Curvature explosion in quotients and applications*, J. Differential Geom., 85 (2010), pp. 117–140.
24. N. MIOLANE AND X. PENNEC, *Biased estimators on quotient spaces*, Proceedings of the 2nd international of Geometric Science of Information (GSI’2015), (2015).
25. V. PATRANGENARY AND L. ELLINGSON, *Nonparametric Statistics on Manifolds and Their Applications to Object Data Analysis*, Taylor & Francis group, 2016.
26. X. PENNEC, *Toward a generic framework for recognition based on uncertain geometric features*, Videre: Journal of Computer Vision Research, 1 (1998), pp. 58–87.
27. X. PENNEC, *Intrinsic statistics on Riemannian manifolds: Basic tools for geometric measurements*, Journal of Mathematical Imaging and Vision, 25 (2006), pp. 127–154.
28. X. PENNEC AND N. AYACHE, *A geometric algorithm to find small but highly similar 3d substructures in proteins.*, Bioinformatics, 14 (1998), pp. 516–522.
29. M. POSTNIKOV, *Riemannian Geometry*, Encyclopaedia of Mathem. Sciences, Springer, 2001.
30. RSTUDIO, INC, *Easy web applications in R.*, 2013. URL: <http://www.rstudio.com/shiny/>.

31. I. J. TICKLE, R. A. LASKOWSKI, AND D. S. MOSS, *Error Estimates of Protein Structure Coordinates and Deviations from Standard Geometry by Full-Matrix Refinement of γ B- and β B2-Crystallin*, Acta Crystallographica Section D, 54 (1998), pp. 243–252.
32. L. YOUNES, *Shapes and Diffeomorphisms*, Applied Mathematical Sciences, Springer London, Limited, 2012.

A Proofs of the theorems

Here X is a point in M . We consider that X belongs to a principal orbit $O = O_X$. This will have no impact on the integration because the set of principal orbits is dense in M . We write $\pi(X)$ the projection of X in the shape space.

We write the template shape Y . We write its estimate \hat{Y} . We take a normal coordinate system centered at the template Y . We have the decomposition $X = (X_O, X_H) \in T_Y O \oplus H$, where O is the orbit of Y . We note that $\pi(X) \neq \text{Exp}_Y X_H$, so that X_H are *not* the coordinates of $\pi(X)$ in the normal coordinate system at Y , see Figure 22.

We denote m the dimension of M , p the dimension of the principal orbits and q the dimension of the quotient space. We write coordinates in Q with indices $a, b, \dots \in [1, q]$ and coordinates in an orbit with indices $i, j, \dots \in [1, p]$.

The generative model implies the following Riemannian normal distribution on the objects:

$$F(X) = \frac{1}{C_M(\sigma)} \exp\left(-\frac{d_M^2(X, Y)}{2\sigma^2}\right) \quad \text{with} \quad C_M(\sigma) = \int_M \exp\left(-\frac{d_M^2(X, Y)}{2\sigma^2}\right) dM(X). \quad (11)$$

The distance $d_M(X, Y)$ expressed in the normal coordinate system at Y is simply $d_M(X, Y)^2 = X^T X$. The Riemannian measure $dM(X)$ at X in the normal coordinate system at Y has the Taylor expansion: $dM(X) = dX - \frac{1}{6} \sum_{A,B,C} R_{ABAC} X^B X^C dX + \mathcal{O}(\|X\|^3)$. We recognize the Riemannian curvature tensor R .

We truncate the Riemannian Gaussian:

$$F(X) = \frac{1}{S^m(\sqrt{2\pi})^m \sigma^m} \exp\left(-\frac{X^T X}{2\sigma^2}\right), \quad (12)$$

where S is the normalization coefficient coming of the univariate truncated Gaussian at $\sigma/2$. B_M , B_O and B_Q refer to geodesic balls of radius $\sigma/2$ in their respective spaces. We denote $C_M = S^m(\sqrt{2\pi})^m \sigma^m$ and remark that $C_M = C_H C_O = S^q(\sqrt{2\pi})^q \sigma^q \cdot S^p(\sqrt{2\pi})^p \sigma^p$ where q is the dimension of the quotient space and p the dimension of the principal orbits.

In the following 'NCS' means 'normal coordinate system'.

A.1 Proof a lemma.

Lemma 1. *The coordinates of $\pi(X)$ in a NCS at $T_Y M$ are:*

$$\pi(X)_H = X_H - \frac{1}{2} X_O^T \cdot h(X) \cdot X_O + \mathcal{O}(\|X_O\|^3), \quad \text{and} \quad \pi(X)_O = 0.$$

Proof. We represent O in $T_{\pi(X)} M$ as the graph of a smooth function from $T_{\pi(X)} O$ to $N_{\pi(X)} O$, around $X_O = 0$ by:

$$\begin{aligned} I : T_{\pi(X)} O &\mapsto T_X M = T_{\pi(X)} O \oplus N_{\pi(X)} O \\ X_O &\mapsto I(X_O) = (X_O, G(X_O)). \end{aligned}$$

The local graph G is: $G(X_O) = -\frac{1}{2} X_O^T \cdot h(X) \cdot X_O + \mathcal{O}(\|X_O\|^3)$. Its 0-th and 1-th order derivatives are zero because the graph goes through $\pi(X)$ and is tangent at $T_{\pi(X)} O$. Its second order derivative is $h(X)$ and represents the best quadratic approximation of the graph.

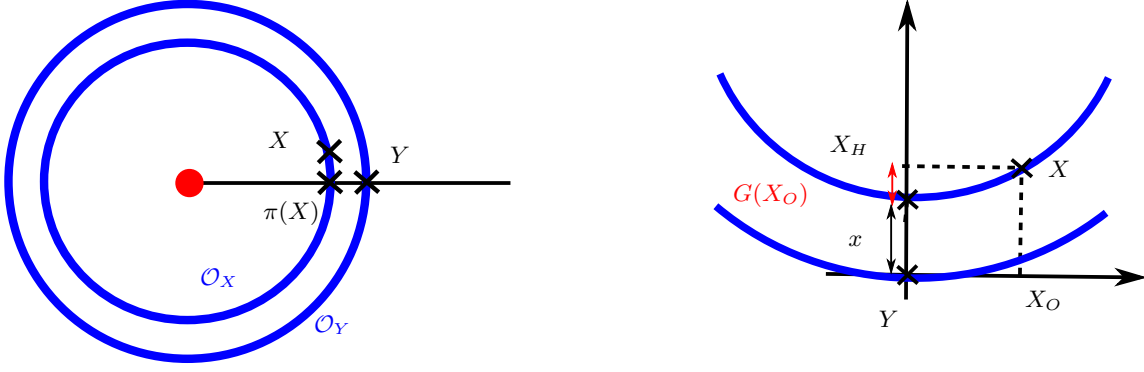


Fig. 22. Summary of the notations used in the proofs.

The coordinate of $\text{Exp}_Y X_H$ in a NCS centered at $\pi(X)$ is $G(X_O)$. Conversely, the coordinate of $\pi(X)$ in a normal coordinate system centered at $\text{Exp}_Y X_H$ is $-G(X_O)$.

We need the coordinate of $\pi(X)$ in the NCS at Y . We parallel transport $-G(X_O)$ from $\text{Exp}_Y X_H$ to Y : $\pi(X)_H = X_H + \Pi(-G(X_O))_{\rightarrow Y}$. The 0-th order term of the parallel transport at $\text{Exp}_Y X_H$ in a NCS at Y is 0:

$$\Pi(-G(X_O))_{\rightarrow Y} = -G(X_O) + \mathcal{O}(\|X_O\|^3).$$

This concludes. □

A.2 Proof of Theorem 1

Proof. We take an NCS at Y . We denote x the coordinate of $\pi(X)$ in the shape space. We compute the induced probability distribution f on shapes by integrating the distribution on the orbit of X out of $F(X)$:

$$f(x) = \frac{1}{C_M} \int_{B_O} \exp\left(-\frac{d_M^2(Y, X)^2}{2\sigma^2}\right) dO(X_O).$$

The point X has coordinates $(X_O, x + G(X_O))$ where X_O is the integration coordinate.

$$\begin{aligned} d_M^2(Y, X) &= x^T x + X_O^T X_O - \frac{1}{2} \sum_a X_O^T h_a(x) X_O x_a + \mathcal{O}(\|X_O\|^3), \\ \Rightarrow \exp(d_M^2(Y, X)) &= \exp\left(-\frac{x^T x}{2\sigma^2}\right) \left(1 + X_O^T X_O - \frac{1}{2} \sum_a X_O^T h_a(x) X_O x_a + \mathcal{O}(\|X_O\|^3)\right). \end{aligned}$$

Plugging this into the expression of the induced probability distribution function gives:

$$\begin{aligned} f(x) &= \frac{1}{C_M} \exp\left(-\frac{x^T x}{2\sigma^2}\right) \int_{B_O} \left(1 + X_O^T X_O - \frac{1}{2} \sum_a X_O^T h_a(x) X_O x_a + \mathcal{O}(\|X_O\|^3)\right) dO(X_O) \\ &= \frac{1}{C_H} \exp\left(-\frac{x^T x}{2\sigma^2}\right) ((1) + (2) + (3)), \end{aligned}$$

where:

$$\begin{aligned}
(1) &= \frac{1}{C_O} \int_{B_O} dO(X_O), \\
(2) &= x_a \sum_{ij} \left(\delta_{ij} - \frac{1}{2} h_{ij}(x) \right) \frac{1}{C_O} \int_{B_O} X_{O_i} X_{O_j} dO(X_O), \\
(3) &= \frac{1}{C_O} \int_{B_O} \mathcal{O}(\|X_O\|^3) dO(X_O).
\end{aligned}$$

The Lie group action is isometric so the Riemannian metric splits onto $T_X H \oplus T_X O$ at any point. Moreover, the Taylor expansion of the metric around X still respects the splitting at the third order. The measure $dO(X_O)$ for X_O close enough to X is the restriction of this Taylor expansion to the orbit. We have:

$$g^O(X_O)_{ij} = g^O(X)_{ij} - \sum_{k,l} \frac{1}{3} R_{ikjl}^O X_O^k X_O^l + \mathcal{O}(\|X_O\|^3), \quad (13)$$

so that: $dO(X_O) = \sqrt{|\det(g^O(X_O)_{ij})|} dX_O = dX_O - \frac{1}{6} \sum_{k,l} R_{kl}^O X_O^k X_O^l dX_O + \mathcal{O}(\|X_O^3\|)$ where R is the Ricci curvature.

We recognize a moment in (1) and (2), so that:

$$\begin{aligned}
(1) &= \frac{1}{C_O} \int_{B_O} dO(X_O) \\
&= \frac{1}{C_O} \int_{B_O} \left(1 - \frac{1}{6} \sum_{k,l} R_{kl}^O X_O^k X_O^l + \mathcal{O}(\|X_O^3\|) \right) dX_O \\
&= c_p^0 - \frac{1}{6} \sum_{k,l} R_{kl}^O \frac{\sigma^2}{(\sqrt{2\pi})^p S^p} \\
(2) &= x_a \sum_{ij} \left(\delta_{ij} - \frac{1}{2} h_{ij}(x) \right) \frac{1}{C_O} \int_{B_O} X_{O_i} X_{O_j} dX_O \\
&= x_a \sum_{ij} \left(\delta_{ij} - \frac{1}{2} h_{ij}(x) \right) \frac{\sigma^2}{(\sqrt{2\pi})^p S^p}.
\end{aligned}$$

We denote $c_p = \frac{1}{(\sqrt{2\pi})^p S^p}$.

For the last term (3), we assume again that the graph of the orbit is smooth enough so that it admits a Taylor serie at $X_O = 0$, ie: $\mathcal{O}(\|X_O\|^3) = \sum_{k=3}^{\infty} \sum_{i_1, \dots, i_k} c_{k,X} X_{O_{i_1}} \dots X_{O_{i_k}}$. By plugging this, we get the moments with the same manipulation as in the proof of Theorem 1. As the moments of order 3 (and of odd order) are zero: $(3) = \mathcal{O}(\sigma^4)$.

Gathering the results gives:

$$f(x) = \frac{1}{C_H} \exp \left(-\frac{x^T x}{2\sigma^2} \right) \left(c_p^0 + c_p \sum_{ij} \left(\delta_{ij} - \frac{1}{6} R_{ij}^O - \sum_a \frac{1}{2} h_{ij}^a(x) x_a \right) \sigma^2 + \mathcal{O}(\sigma^4) \right).$$

□

A.3 Proof of Theorem 2

Proof. We show this result for a multivariate truncated Gaussian at $\sigma/2$ in each coordinate. We call S the coefficient of the univariate truncated Gaussian at $\sigma/2$.

We want to compute the systematic bias. To this aim, we compute the mean of the distribution of shapes in Q , in a coordinate system centered at the real Y . It writes:

$$\text{Bias}(Y, \hat{Y}) = \frac{1}{C_M} \int_{B_M} \pi(X) \exp\left(-\frac{X^T X}{2\sigma^2}\right) dM(X). \quad (14)$$

The coordinates of X in the Euclidean coordinate system at Y are simply (X_O, X_H) . Thus $d_M^2(Y, X) = X_H^T X_H + X_O^T X_O$. From the lemma above:

$$\pi(X) = (0, X_H + \frac{1}{2} X_O^T h(x) X_O + \mathcal{O}(\|X_O\|^3)). \quad (15)$$

We plug this in the integral, to get:

$$\text{Bias}(Y, \hat{Y}) = \frac{1}{C_M} \int_{B_M} \left(X_H + \frac{1}{2} X_O^T h(x) X_O + \mathcal{O}(\|X_O\|^3) \right) \cdot \exp\left(-\frac{X_H^T X_H + X_O^T X_O}{2\sigma^2}\right) dX,$$

where only the 0-th order of the volume element expansion $dM(X) = dX + \mathcal{O}(\|X\|^2)$ matters.

Integrating the element X_H on the centered Gaussian gives 0:

$$\begin{aligned} \text{Bias}(Y, \hat{Y}) &= \frac{1}{C_M} \int_{B_M} \frac{1}{2} X_O^T h(x) X_O \exp\left(-\frac{X_H^T X_H + X_O^T X_O}{2\sigma^2}\right) dX_H dX_O \\ &\quad + \frac{1}{C_M} \int_{B_M} \mathcal{O}(\|X_O\|^3) \exp\left(-\frac{X_H^T X_H + X_O^T X_O}{2\sigma^2}\right) dX_H dX_O. \end{aligned}$$

We denote (1) the first term of the sum and (2) the second term of the sum. We compute them independently.

$$\begin{aligned} (1) &= \frac{1}{2C_M} \sum_{i,j} \int_{B_Q} h_{ij}(x) \left(\int_{B_O} X_{Oi} X_{Oj} \exp\left(-\frac{X_O^T X_O}{2\sigma^2}\right) dX_O \right) \exp\left(-\frac{X_H^T X_H}{2\sigma^2}\right) dX_H \\ &= \frac{1}{2C_H} \sum_{i,j} \int_{B_Q} h_{ij}(x) \left(\frac{1}{C_O} \int_{B_O} X_{Oi} X_{Oj} \exp\left(-\frac{X_O^T X_O}{2\sigma^2}\right) dX_O \right) \exp\left(-\frac{X_H^T X_H}{2\sigma^2}\right) dX_H \\ &= \frac{\sigma^2(1+\kappa)}{2C_H} \sum_{i,j} \int_{B_Q} h_{ij}(x) \delta_{ij} \exp\left(-\frac{X_H^T X_H}{2\sigma^2}\right) dX_H, \end{aligned}$$

where the last line comes from the definitions of the moments of the truncated Gaussian.

We recognize the definition of the trace:

$$\begin{aligned} (1) &= \frac{\sigma^2(1+\kappa)}{2C_H} \sum_i \int_{B_Q} h_{ii}(x) \exp\left(-\frac{X_H^T X_H}{2\sigma^2}\right) dX_H \\ &= \frac{\sigma^2(1+\kappa)}{2C_H} \int_{B_Q} H(x) \exp\left(-\frac{X_H^T X_H}{2\sigma^2}\right) dX_H. \end{aligned}$$

We perform a change of variable in the integral $X_H \rightarrow X'_H$ so that $X_H = \sigma X'_H$, $x = \sigma x'$ and $dX_H = \sigma^q dX'_H$. This gives:

$$(1) = \frac{\sigma^2(1+\kappa)}{2C_H} \int_{B_Q} H(\sigma x') \exp\left(-\frac{X_H^T X_H}{2}\right) dX_H.$$

We perform a Taylor expansion under the integration, in σ , using the chain rule:

$$(1) = \frac{\sigma^2(1+\kappa)}{2C_H} \int_{B_Q} \left(H(0) + \sum_{a=1}^q x'_a \frac{\partial H}{\partial x'_a}(0) \sigma + \mathcal{O}(\sigma^2) \right) \exp \left(-\frac{X_H^T X_H}{2} \right) dX_H.$$

Again, the terms in X_{H_a}' integrate to 0. We have:

$$\begin{aligned} (1) &= \frac{\sigma^2(1+\kappa)}{2C_H} \int_{B_Q} H(0) \exp \left(-\frac{X_H^T X_H}{2} \right) dX_H + \mathcal{O}(\sigma^4) \\ &= H(0) \frac{\sigma^2(1+\kappa)}{2C_H} \int_{B_Q} \exp \left(-\frac{X_H^T X_H}{2} \right) dX_H + \mathcal{O}(\sigma^4). \end{aligned}$$

The term $\int_{B_Q} \exp \left(-\frac{X_H^T X_H}{2} \right) dX_H$ is precisely the normalization constant of the truncated Gaussian $C_H = S^q(\sqrt{2\pi})^q$, so that:

$$(1) = H(0) \frac{\sigma^2(1+\kappa)}{2} + \mathcal{O}(\sigma^4).$$

The coefficient κ comes from the fact that we have truncated the Gaussian. Its expression is independent of σ because we have truncated at a multiple of σ . Now we show that the second term (2) is of order σ^4 .

$$(2) = \frac{1}{C_M} \int_{B_M} \mathcal{O}_X(\|X_O\|^3) \exp \left(-\frac{X_H^T X_H + X_O^T X_O}{2\sigma^2} \right) dX_H dX_O.$$

We assume that the local graph of the orbit is smooth enough so that it has a multivariate Taylor serie: $\mathcal{O}(\|X_O\|^3) = \sum_{k=3}^{\infty} \sum_{i_1, \dots, i_k} c_{k,X} X_{O_{i_1}} \dots X_{O_{i_k}}$. We have:

$$(2) = \frac{1}{C_M} \int_{B_M} \left(\sum_{k=3}^{\infty} \sum_{i_1, \dots, i_k} c_{k,X} X_{O_{i_1}} \dots X_{O_{i_k}} \right) \exp \left(-\frac{X_H^T X_H + X_O^T X_O}{2\sigma^2} \right) dX_H dX_O.$$

Here the c_k depend on X_H . We first perform a majoration on each on them by a C_k (integration on a compact ball).

$$\begin{aligned} \|(2)\| &\leq \frac{1}{C_M} \sum_{k=3}^{\infty} C_k \sum_{i_1, \dots, i_k} \int_{B_H} \left\| \int_{B_O} X_{O_{i_1}} \dots X_{O_{i_k}} \exp \left(-\frac{X_H^T X_H + X_O^T X_O}{2\sigma^2} \right) dX_O \right\| dX_H \\ &= \frac{1}{C_M} \sum_{k=3}^{\infty} C_k \sum_{i_1, \dots, i_k} \int_{B_H} \exp \left(-\frac{X_H^T X_H}{2\sigma^2} \right) dX_H \cdot \left\| \int_{B_O} X_{O_{i_1}} \dots X_{O_{i_k}} \exp \left(-\frac{X_O^T X_O}{2\sigma^2} \right) dX_O \right\|. \end{aligned}$$

We compute: $\int_{B_Q} \exp \left(-\frac{X_H^T X_H}{2\sigma^2} \right) dX_H = C_H$ so that:

$$\begin{aligned} \|(2)\| &\leq \frac{1}{C_O} \sum_{k=3}^{\infty} C_k \sum_{i_1, \dots, i_k} \left\| \int_{B_O} X_{O_{i_1}} \dots X_{O_{i_k}} \exp \left(-\frac{X_O^T X_O}{2\sigma^2} \right) dX_O \right\| \\ &= \sum_{k=3}^{\infty} C_k \sum_{i_1, \dots, i_k} \frac{1}{C_O} \left\| \int_{B_O} X_{O_{i_1}} \dots X_{O_{i_k}} \exp \left(-\frac{X_O^T X_O}{2\sigma^2} \right) dX_O \right\|, \end{aligned}$$

where we recognize the moment of the truncated Gaussian, which are non zero only for even power. This gives: $(2) = \mathcal{O}(\sigma^4)$.

Gathering the computations of (1) and (2), we get the formula of the bias:

$$\text{Bias}(Y, \hat{Y}) = H(0) \frac{\sigma^2(1 + \kappa)}{2} + \mathcal{O}(\sigma^4).$$

□